




# JGR Solid Earth

## RESEARCH ARTICLE

10.1029/2023JB028073

## Stress Balance in Synthetic Serpentinized Peridotites Deformed at Subduction Zone Pressures

N. Hilairret<sup>1</sup> , J. Guignard<sup>2,3</sup>, T. P. Ferrand<sup>4,5</sup> , S. Merkel<sup>1</sup> , P. Raterron<sup>1,6</sup>, B. Ildefonse<sup>7</sup> , A. Fadel<sup>8</sup>, and W. Crichton<sup>2</sup>

### Key Points:

- In situ stresses within antigorite + olivine aggregates deformed under high pressures and temperatures
- Stress partitioning changes with a threshold between 10% and 20 % antigorite volume fraction
- Olivine controls stress before this threshold and the aggregate hardens relative to pure olivine

### Supporting Information:

Supporting Information may be found in the online version of this article.

### Correspondence to:

N. Hilairret,  
nadege.hilairret@univ-lille.fr

### Citation:

Hilairret, N., Guignard, J., Ferrand, T. P., Merkel, S., Raterron, P., Ildefonse, B., et al. (2024). Stress balance in synthetic serpentinized peridotites deformed at subduction zone pressures. *Journal of Geophysical Research: Solid Earth*, 129, e2023JB028073. <https://doi.org/10.1029/2023JB028073>

Received 13 OCT 2023

Accepted 23 JAN 2024

### Author Contributions:

**Conceptualization:** N. Hilairret  
**Data curation:** N. Hilairret  
**Formal analysis:** N. Hilairret  
**Funding acquisition:** N. Hilairret  
**Investigation:** N. Hilairret, J. Guignard, T. P. Ferrand, S. Merkel, P. Raterron, B. Ildefonse, A. Fadel, W. Crichton  
**Methodology:** N. Hilairret  
**Project administration:** N. Hilairret  
**Resources:** N. Hilairret, S. Merkel, B. Ildefonse, W. Crichton  
**Software:** N. Hilairret, S. Merkel, B. Ildefonse  
**Validation:** N. Hilairret  
**Writing – original draft:** N. Hilairret

© 2024. The Authors.

This is an open access article under the terms of the [Creative Commons Attribution-NonCommercial-NoDerivs License](https://creativecommons.org/licenses/by/4.0/), which permits use and distribution in any medium, provided the original work is properly cited, the use is non-commercial and no modifications or adaptations are made.

<sup>1</sup>Univ. Lille, CNRS, INRAE, Centrale Lille, UMR 8207 - UMET - Unité Matériaux et Transformations, Lille, France, <sup>2</sup>ESRF European Synchrotron, Grenoble, France, <sup>3</sup>Now at IROX Technology, Toulouse, France, <sup>4</sup>PSL Research University, Laboratoire de Géologie, Ecole Normale Supérieure, Paris, France, <sup>5</sup>Institute of Geological Sciences, Freie Universität Berlin, Berlin, Germany, <sup>6</sup>Now at National Science Foundation, Alexandria, VA, USA, <sup>7</sup>Geosciences Montpellier, University of Montpellier, CNRS, Montpellier, France, <sup>8</sup>University Lille, CNRS, INRAE, Centrale Lille, Université d'Artois, FR 2638 - IMEC - Institut Michel-Eugène Chevreul, Lille, France

**Abstract** Weak serpentine minerals affect the mechanical behavior of serpentinized peridotites at depth, and may play a significant role in deformation localization within subduction zones, at local or regional scale. Mixtures of olivine with 5, 10, 20 and 50 vol. % fraction of antigorite, proxies for serpentinized peridotites, were deformed in axial shortening geometry under high pressures (ca. 2–5 GPa) and moderate temperatures (ca. 350° C), with in situ stress and strain measurements using synchrotron X-rays. We evaluate the average partitioning of stresses at the grains scale within each phase (mineral) of the aggregate and compare with pure olivine aggregates in the same conditions. The in situ stress balance is different between low antigorite contents up to 10 vol. %, and higher contents above 20 vol. %. Microstructure and stress levels suggest the deformation mechanisms under these experimental conditions are akin to (semi)brittle and frictional processes. Unlike when close to dehydration temperatures, hardening of the aggregate is observed at low serpentine fractions, due to an increase in local stress concentrations. Below and above the 10–20 vol. % threshold, the stress state in the aggregate corresponds to friction laws already measured for pure olivine aggregates and pure antigorite aggregates respectively. As expected, the behavior of the two-phase aggregate does not evolve as calculated from simple iso-stress or iso-strain bounds, and calls for more advanced physical models of two-phase mixtures.

**Plain Language Summary** In subduction zones, a tectonic plate plunges beneath another one, and result in large mechanical stresses. These conditions can lead to earthquakes or ground displacements observable at human timescales. Measuring how viscous the rocks within subduction zones are, may help understand these events. Serpentine are rocks from subduction zones which contain a variable amount of a weak minerals, including serpentine, and other stronger minerals. Using deformation experiments this study seeks to measure serpentine viscosity, as a function of the amount of serpentine. At low serpentine content (at least up to 10%, but lower than 20 vol.%) and under temperature relevant for cold subduction zones, we found that the rock remains as hard as the strongest mineral which bears the whole load, and can even become harder because of grain-scale stress concentrations. At 50% volume fraction of serpentine, the rock has the same viscosity as serpentine itself. These measurements may for instance help larger scale numerical models of interseismic processes that happen between earthquakes, in subduction zones.

## 1. Introduction

Understanding strain localization processes within subduction zones, from long timescales (convection) to intermediate scales (slow slip events over hours or days), to short events (earthquakes) has become of major importance for our global picture of subduction zones dynamics. However, the strain rates and the stress balance at the interface between the slab and the mantle wedge, as well as those in the inner part of the subducting slab, remain poorly quantified. Rheological contrasts between different lithologies are decisive for the dynamics at the interface, including the exhumation of high pressure rocks (e.g., Agard et al., 2018 for a review, Schwartz et al., 2001; Federico et al., 2007), as well as seismicity (e.g., Ferrand, 2019, observations in Abers et al., 2013) and mantle wedge flow (e.g., Abers et al., 2006; Wada et al., 2008). Knowledge of the rheology of subduction zones lithologies is thus required in order to decipher their histories and present-day processes.

Writing – review & editing: N. Hilaret,  
J. Guignard, T. P. Ferrand, S. Merkel,  
B. Ildefonse, W. Crichton

Serpentinized rocks have long been proposed to strongly influence subduction zones dynamics, through a low mechanical strength (e.g., Guillot et al., 2015 and ref. therein, Schwartz et al., 2001). Serpentinization is a partial or total replacement of the most abundant silicate in peridotites, olivine, and pyroxene to a lesser extent, as a result of hydration. Antigorite, the high-pressure, high-temperature (above ca. 300°C) variety of serpentine (e.g., Evans, 2004; Schwartz et al., 2013) is potentially widespread in the mantle above the subduction interface, where fluids are released by progressive dehydration of hydrous phases in the subducting slab (e.g., Schmidt & Poli, 1998).

The rheological behavior of fresh dunite and peridotites, or olivine aggregates under high pressure - low temperatures below and up to 600°C, has been investigated for decades (e.g., Boettcher et al., 2007; Druiventak et al., 2011; Gaboriaud et al., 1981; Long et al., 2011; Mei et al., 2010; Proietti et al., 2016; Raterron et al., 2004; Shimada et al., 1983). The rheology of serpentine aggregates and natural serpentinites has been studied under pressures up to 4 GPa and from ambient temperature up to dehydration temperatures (e.g., Burdette & Hirth, 2022; Chernak & Hirth, 2010; Escartin et al., 1997; Hilaret et al., 2007; Hirauchi et al., 2020; Proctor & Hirth, 2016; Shao et al., 2021). At single-crystal scale, olivine mechanical properties have also been investigated under low temperatures (e.g., Evans & Goetze, 1979; Gaboriaud et al., 1981; Idrissi et al., 2016; Kranjc et al., 2016; Kumamoto et al., 2017), and more recently those of antigorite (Hansen et al., 2020; Idrissi et al., 2020).

On the other hand, the mechanical behavior of serpentinized rocks has not been systematically investigated. Experiments have been carried out mostly under pressures below 2 GPa on the low temperature serpentine varieties lizardite and chrysotile (e.g., Escartin et al., 2001). High pressure experiments on antigorite-olivine aggregates or antigorite-rich serpentinites have mostly been targeted at antigorite dehydration conditions, owing to its potential link with subduction zone seismicity (e.g., Chernak & Hirth, 2011; Dobson et al., 2002; Ferrand, 2017; Ferrand et al., 2017; Gasc et al., 2011, 2017; Jung & Green, 2004; Xia, 2013).

Olivine and serpentine have different intrinsic elastic and crystal-plastic properties. Therefore the resulting elastic and plastic properties of the serpentinites may not be easily predicted from the end-members (in the following, “plastic properties” refers to crystal plastic properties unless otherwise stated). Burnley (2013) for instance, modeled how contrasts in elastic and plastic properties can lead to variable local stress states, due to stress percolation.

Microstructure is also expected to influence stress distribution throughout a deforming two-phase aggregate. Indeed, serpentinites can be found within heterogeneously deformed shear zones and tend to have strong preferred orientations (e.g., Morales et al., 2018; Nishii et al., 2011; Padron-Navarta et al., 2012). Handy (1990, 1994), laid out a conceptual framework with two end-members 1) the strongest phase controls the stress through a load-bearing framework 2) the weakest phase controls deformation because it is spatially connected, being either abundant enough to be connected prior to deformation, or becoming connected through increasing strain amount. More recently Gerbi et al. (2016), underlined that beyond the simple connectivity of weak phases in natural rocks, development of weak “bridging” zones can control the aggregate strength.

Analytical mixing models, ranging from simple end-member models to more complex models, do exist for flow laws (e.g., Huet et al., 2014; Takeda, 1998; Tullis et al., 1991), but are not easily applicable when frictional processes and semi-brittle deformation occur. A wealth of numerical studies on two-phase geological aggregates is available in the literature, based one way or the other on Finite Elements Models (e.g., Cook et al., 2014; Cyprych et al., 2016; Jessell et al., 2009; Madi et al., 2005; Tullis et al., 1991), sometimes combined with mean-field or analytical approaches (e.g., Canova et al., 1992; Thielmann et al., 2020). These numerical models remain costly computationally and need anchoring on observables and experimental work in order to be relevant and well-targeted. Experimental mapping of physical (pressure, temperature, strain rate, strain) and microstructural conditions for specific deformation regimes of serpentinites is therefore necessary.

A number of studies have taken advantage of high-pressure deformation experiments with in situ synchrotron X-ray measurements in two-phase mineralogical assemblages, which allow to investigate the stress partitioning between the different phases (Farla et al., 2017; Girard et al., 2016; Kaercher et al., 2016; Li et al., 2007; Lin et al., 2019; Tokle et al., 2021; Wang et al., 2013). We present here an experimental study of the effect of serpentine fraction within a mixture of olivine + antigorite, on the mechanical behavior of the aggregate. The deformation experiments were carried out under high pressure and high temperature, in axisymmetric shortening

**Table 1**  
*Summary of Experimental Runs Conditions*

Run #	atg vol. % in two phase aggr.	Strain rate ref.	Final strain ref.	Strain rate two-phase aggr.	Final strain two-phases aggr.	$\sigma_{ol}$ ref. (GPa) <sup>a</sup>	P ref. (GPa) <sup>b</sup>	$\sigma_{ol}$ two-phase aggr. (GPa) <sup>a</sup>	P two-phase aggr. (GPa) <sup>b</sup>	$\sigma_{atg(001)}$ (GPa)	Peak $\sigma_{atg(001)}$ (GPa)
serp6	0.05	-1.99E-05	-0.23	-1.58E-05	-0.20	3.78	4.86	3.69	4.91	1.06	2.18
serp7	0.1	-1.43E-05	-0.25	-1.66E-05	-0.29	3.73	4.00	3.49	4.00	1.68	2.58
serp9	0.2	-1.17E-05	-0.14	-4.52E-05	-0.27	3.23	1.89	3.02	1.78	2.84	2.84
serp10	0.5	-1.77E-05	-0.19	-3.61E-05	-0.34	3.25	3.18	2.67	3.17	2.64	2.64

<sup>a</sup>Stress calculated from olivine diffraction planes. Standard deviations: See data set, Hilairet et al. (2024). <sup>b</sup>P measured from olivine diffraction, given here at the final strain.

(pure shear). Using in situ stresses and strain measurements, we evaluate the partitioning of stresses within each phase (mineral) of the aggregate. These results show two distinct regimes for stress partitioning as a function of the antigorite volume fraction, with different mechanisms for stress control.

## 2. Methods

The deformation experiments were carried out in the D-DIA large-volume press at ID6-LVP at the European Synchrotron Radiation Facility in Grenoble, France (Guignard & Crichton, 2015). A monochromatic beam with a wavelength corresponding to 33 keV was used, with a beam size of ca. 1 mm wide by 0.5 mm height.

The samples were powders ground and mixed from natural San Carlos olivine and antigorite from Corsica, used in Ferrand et al. (2017) and Ferrand (2017) with 5, 10, 20 and 50 vol. % antigorite. The powders were sieved for grain sizes below ca. 30 microns. Upon compression under high pressure (P) and high temperature (T) (1.5 GPa, 773K), the resulting aggregates display a rather homogeneous distribution of the phases (Ferrand, 2017). Antigorite is distributed in patches, referred to as “clusters” in Ferrand et al. (2017), that become connected at the highest antigorite fraction. In the present experiments the mixtures were hand-pressed and directly loaded within the high-pressure cells.

Anvils with 6 mm truncation were used, made of tungsten carbide on the upstream side and sintered diamond (SD) on the downstream side, for recovering full angular dispersive diffraction patterns. 9 mm edge cubic cells were used (Figure S1 in Supporting Information S1), with amorphous B + epoxy as pressure medium, a graphite furnace, porous alumina pistons, and zirconia plugs for thermal insulation. In each run, two samples were stacked in the cell: ca. 1.5 mm height, pure olivine powder, and ca. 1.5 mm height, two-phase powder (antigorite + olivine). The pure olivine powder is used as a reference in the same P and T conditions as each two-phase aggregate, in order to compare runs between themselves. All samples were separated from one another and from the pistons by 20 microns-thick gold foils.

The samples were compressed at a target load of 30 bars, intended to reach hydrostatic P ca. 3 GPa (not always reached, see Table 1). The temperature was imposed by a current circulating through a graphite furnace and estimated from an off-line calibration, between 395 and 420°C at the beginning. The shortening of the assembly during deformation in the D-DIA can induce changes in the T gradient (Raterron et al., 2013). Based on their results (at 1673 K, much higher than the present study) and the total length of our samples, here a temperature of 300–350°C is assumed. The stresses built-up during compression were relaxed at the run T for about 1 hr prior to deformation. The samples were then shortened up to the final strain, quenched and decompressed, and finally recovered for SEM analysis.

Sample axial strains were measured using X-ray radiography. Due to the x-ray beam height of 0.5 mm, the samples stacks were scanned in the vertical direction to take a series of 12 or more images, and the full image was reconstructed. One full image was typically acquired over a few seconds, which remains very short with respect to the speed of deformation. The strain is defined as  $\epsilon = \ln(l/l_0)$ ,  $l$  being the sample length and  $l_0$  the reference length taken at the beginning of the deformation (start of differential rams). The experiments were carried out at strain rates around  $10^{-5} \text{ s}^{-1}$  and total strains up to ca. 30% (Table 1).

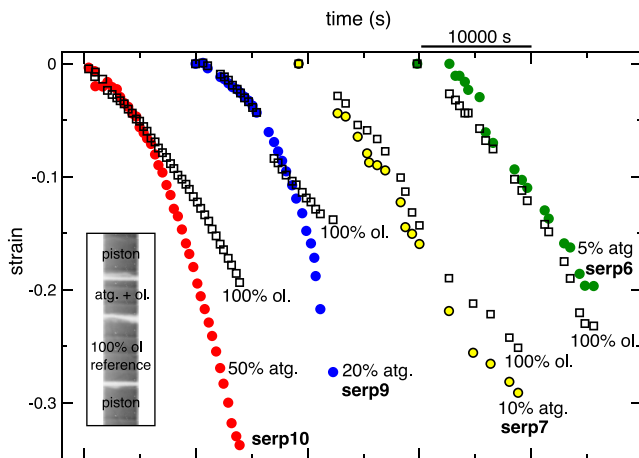


**Figure 1.** Strain evolution with time for the two-phase aggregates (filled symbols) and for the reference (100 vol. % olivine aggregate, empty squares). Each run (serp6, 7, 9, 10) had a reference aggregate in the column stack, as shown in the inset. The curves have been shifted one run from another on the time axis, for visibility. The scatter on runs serp6 and serp7 is due to the image analysis process, which was improved for runs serp 9 and serp10. The jump and change of slope seen on serp9 is real.

2D X-ray diffraction (XRD) patterns were collected on a rotating linear 1-D detector (see Guignard & Crichton, 2015, for details), with a typical acquisition time of the order of 1 min for a 360° full azimuthal acquisition. The detector tilt and rotation relative to the incident beam were calibrated with a LaB<sub>6</sub> standard using Fit2D (Hammersley, 2016). The 2D diffractions allowed recovering stresses within phases in the single-phase and two-phase samples for each run. The full framework for these analyses has been widely presented in the literature (e.g., Singh et al., 1998; Uchida et al., 1996). For a polycrystal under differential stress, departure of the powder diffraction pattern from ideal rings can be used as a proxy for the supported differential stress. This departure is referred to as “lattice strain,” noted  $Q(hkl)$  for the  $hkl$  diffraction line. The isotropic component of the stress tensor (the mean stress), hereafter called either pressure (P) or mean stress, can also be recovered. The analysis was carried out using the Multifit—Polydefix software available online at <http://merkel.zoneo.net/Multifit-Polydefix/> (Merkel & Hilaret, 2015).

P was calculated using a thermal equation of state for San Carlos olivine (Guyot et al., 1996) in the reference sample and in the two-phase sample. Both were fairly consistent (Table 1). Antigorite d-spacings were not converted to pressures because only one diffraction plane with robust information was available.

Converting lattice strains into macroscopic stresses is not straightforward (see Chen et al., 2006; Burnley & Zhang, 2008; Merkel et al., 2009 for a full discussion, and Hilaret et al., 2011 on olivine specifically). Lattice strains from the 021, 101, 130, 131, and 112 diffraction lines (*Pbnm* setting is used throughout the manuscript) were recovered for olivine in both the single-phase aggregates and in the two-phase aggregates. The stresses were calculated from different  $Q(hkl)$  using elastic stiffness tensors ( $C_{ij}$ ) at the relevant P and T (Isaak, 1992; Zha et al., 1996) assuming a constant stress hypothesis (Singh et al., 1998; Uchida et al., 1996). This leads to a spread of stresses calculated from different crystallographic planes, which are then averaged to represent the aggregate stress. This averaging represents the main limitation of in situ stress measurements based on XRD, as it has no theoretical grounds and does not take into account plastic relaxation occurring within the sample. As of today, there is no satisfactory way to obtain the stress uncertainty. Elasto-Visco-Plastic Self-Consistent (EVPSC) modeling of the data has been proposed as an answer to this pitfall (Burnley, 2015; Burnley & Zhang, 2008). The implementation of relevant mechanisms for olivine deformation into these codes, however, is still incomplete (Burnley, 2015; Hilaret et al., 2011). We believe some precautions ensure that relative comparisons can still be made out of these measurements. First, the deformation curves for the four runs display the same relative evolutions for the different planes (not shown), and we compare here averages from the same lattice strains. Second, the texture of the olivine in the aggregates is weak and the diffraction lines include many more crystal orientations than in a strongly textured case. The planes (021), (101), (130), (131), and (112) cover the three main lattice directions in olivine, hence the average is not biased by underrepresented directions of the unit cell.

For antigorite, we recovered lattice strains for the 001 diffraction lines for all two-phase samples. Only pressure dependencies of  $C_{ij}$  for antigorite are available (Bezacier et al., 2010). The expected effect of increasing T would be opposite effect to that of P. Therefore  $C_{ij}$  at ambient P and T were used. This also allows to keep consistency with previous results on antigorite aggregates (Hilaret et al., 2007). Using  $C_{ij}$  at 3 GPa and ambient T increases the calculated  $t(hkl)$  stresses by about 15%, which provides an upper bound for the interpretation of the results.

### 3. Results

The main results from in situ measurements are summarized in Table 1. Olivine and antigorite are referred to as “ol” and “atg” in the table and figures.

#### 3.1. In Situ Strain Rate

The strain rates of the two-phase aggregate with 5 and 10 vol. % and their respective reference aggregates are similar (Figure 1).

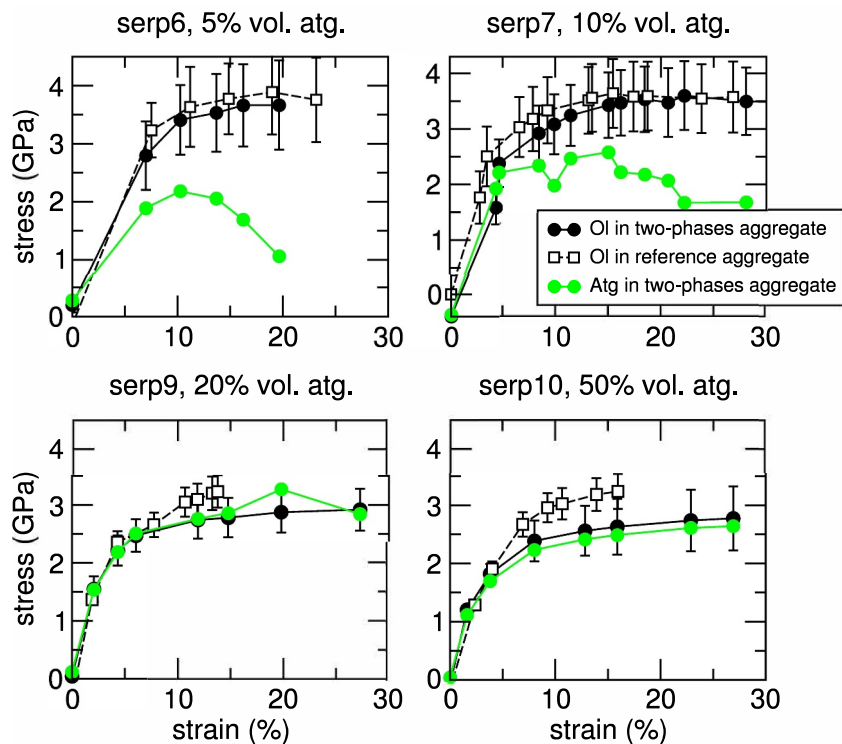


**Figure 2.** Stress partitioning as a function of strain measured in the olivine (ol, solid black circles) and antigorite (atg, green) of the two-phase aggregates, compared to stress - strain curve measured on the olivine single-phase reference aggregate (empty black squares) for each experiment. Stress was not measured for each strain step shown in Figure 1, therefore the final strain shown here can be different. For olivine the stress is calculated from averaging the stress measured on different crystallographic planes. The error from the diffraction fitting is typically the size of the symbols, the bars represent the standard deviation for the average stress (not an actual error on stress, see further information in the methods section). For antigorite, only one plane could be confidently analyzed.

With 20 and 50 vol. % antigorite, the two-phase aggregates deformed faster than the reference aggregate. The speed of the differential rams was identical in all experiments (175  $\mu\text{m}/\text{hour}$ ). The scatter in runs serp6 and serp7 (two-phase and reference aggregate) is due to difficulties in reconstructing an image of the full sample column, from the series of images taken while scanning the column. However, the jump in strain in run serp9 on the olivine reference aggregate is real, and very likely related a failure in the reference aggregate. This is further examined in the discussion.

### 3.2. In Situ Partitioning of Stresses

The diffraction allows us to obtain stress information in each of the two minerals of the two-phase aggregates, which are reported in Figure 2 as stress-strain curves.

Olivine ( $hkl$ ) planes stresses calculated from available lattice strains  $Q(hkl)$  are averaged for clarity. Since the same diffraction planes are considered, and since  $Q(hkl)$  relative amplitudes remain similar, the averaged stresses from the two-phase and the reference aggregates can be compared (also see methods section for stress uncertainty). For the antigorite bearing aggregates, only the basal 001 diffraction peak of antigorite could be confidently fitted. In the 5 vol. % sample, as deformation proceeded the signal on this 001 diffraction line broadened and became too faint to be analyzed.

The 5 and 10 vol. % antigorite aggregates on one side, and the 20 and 50 vol. % antigorite aggregates on the other side, show a different behavior of the (001) plane. The stress on (001) becomes similar to the olivine mean stress when the amount of serpentine is 20% or more. For antigorite-poor aggregates, the stress reaches a maximum and then decreases (Figure 2). The 001 peak then disappears for 5 vol. % antigorite sample, while with the 10 vol. % antigorite, it remains present and reaches a plateau.

### 3.3. Microstructures

In recovered samples, a wide range of brittle features are observed, from micro-cracking, to diffuse or single fracturation at sample scale, sometimes overprinted with unloading cracks. These features are present in single-phase and two-phase aggregates. See Figure S2 in Supporting Information S1 for micrographs of recovered samples. Note the initial angle of any brittle feature generated under high pressure and high temperature may have been altered by the decompression stage, carried out under ambient temperature.

Back-scattered electron images (BSE) were obtained on the recovered samples. This work was carried out at the electron microscopy facility of the Advanced Characterization Platform of the Chevrel Institute, using a FLEXSEM 1000 scanning electron microscope (SEM) (Figure 3), a Hitachi SU 5000 under low-vacuum conditions (Figure 4), and a JEOL JSM-7800F (Figure S2 in Supporting Information S1). Olivine grain sizes in recovered samples range from less than a micron to an apparent equivalent diameter ca. 25–50  $\mu\text{m}$ . BSE images in Figure 3 show the antigorite distribution relative to olivine grains.

Serp6 sample with 5 vol. % antigorite shows no obvious microcracking at the *aggregate scale*. Serp7 sample with 10 vol. % antigorite shows three oblique cracks which seem conjugated and could be related to deformation, without obvious displacements. Openings at grain boundaries, due to the decompression at the end of the run, highlight the cracks. At *crystal scale* olivine presents microcracking in both Serp6 and Serp7 (Figure S3 in Supporting Information S1). Antigorite is distributed as isolated clusters throughout the sample. In these aggregates with 5% and 10% vol. antigorite (serp6, serp7), these clusters tend to have lower aspect ratio than those in the 20 vol. % antigorite sample (Figures 3b and 3d).

Serp 9 with 20 vol. % antigorite, shows only one large crack, not conjugated and with no visible motion, and which geometry is ambiguous to interpret. The distribution of antigorite within the olivine matrix shows clusters of antigorite generally up to 90–100  $\mu\text{m}$  of apparent length on the 2D section, at high angles or perpendicular to the maximum compression axis. One cluster up to 200  $\mu\text{m}$  is observed. The deformation is heterogeneous with some clusters much less deformed in the upper left part of the sample on Figure 3e. As first glance they do not seem to be fully connected across the sample. However, a suite of an-echelon clusters, ca. 500 microns long, is observed in the central part (Figure 3e). The deformation style of antigorite clusters thus evolves with increasing antigorite fraction. The antigorite in the clusters themselves is preserved as crystals of a few microns, with grain size reduction often close to olivine grains (Figure 4a). Some regions with grain size reduction are observed in both in olivine and antigorite (Figure 4b).

Finally, in Serp10 with 50% antigorite, major brittle features allowed a homogeneously distributed (semi-)brittle deformation of the sample. They consist of a regular network of conjugated micro-fractures with a similar apparent angle from the maximum compression axis. At grain scale, the olivine crystals are angular, distributed within an antigorite matrix. Large crystals of antigorite can be preserved, and although grain size reduction is observed, it seems less developed than in serp9. The antigorite clusters deform by grain boundary slip, delamination, kink bands, fracturation, bending (Figures 4d–4f), in response to the local surroundings (relation with olivine crystals Figure 4e).

Reference aggregates in runs serp7 and serp9 display some regions with very small grain sizes (olivine), similar to those observed by Ferrand et al. (2017). Their cause, grain size reduction during deformation or presence from the beginning of the run, is unclear. They are found in olivine reference aggregates only.

The samples have also been investigated by Electron Back-Scattered Diffraction (EBSD)—Scanning Electron Microscopy at the University of Montpellier, on the French CNRS-INSU National EBSD Facility (CamScan Crystal probe). Regions, typically 400 by 500  $\mu\text{m}$ , were mapped for the reference and the two-phase aggregate for each run. Unfortunately, despite several attempts, the EBSD signal on antigorite crystals could not be investigated. This is partly due to the difficulty in polishing the surfaces with such a hardness contrast and with grain sizes approaching the micron - a suitable way of preparing the samples remains to be found. Other likely factors are the deformation mechanisms of antigorite (see discussion). Qualitatively, in situ X-ray diffractions during deformation (not shown) show a lattice preferred orientation for antigorite, with the normals to the basal planes 001 mostly parallel to the maximum compression direction. This texture is stronger at the end of the deformation.

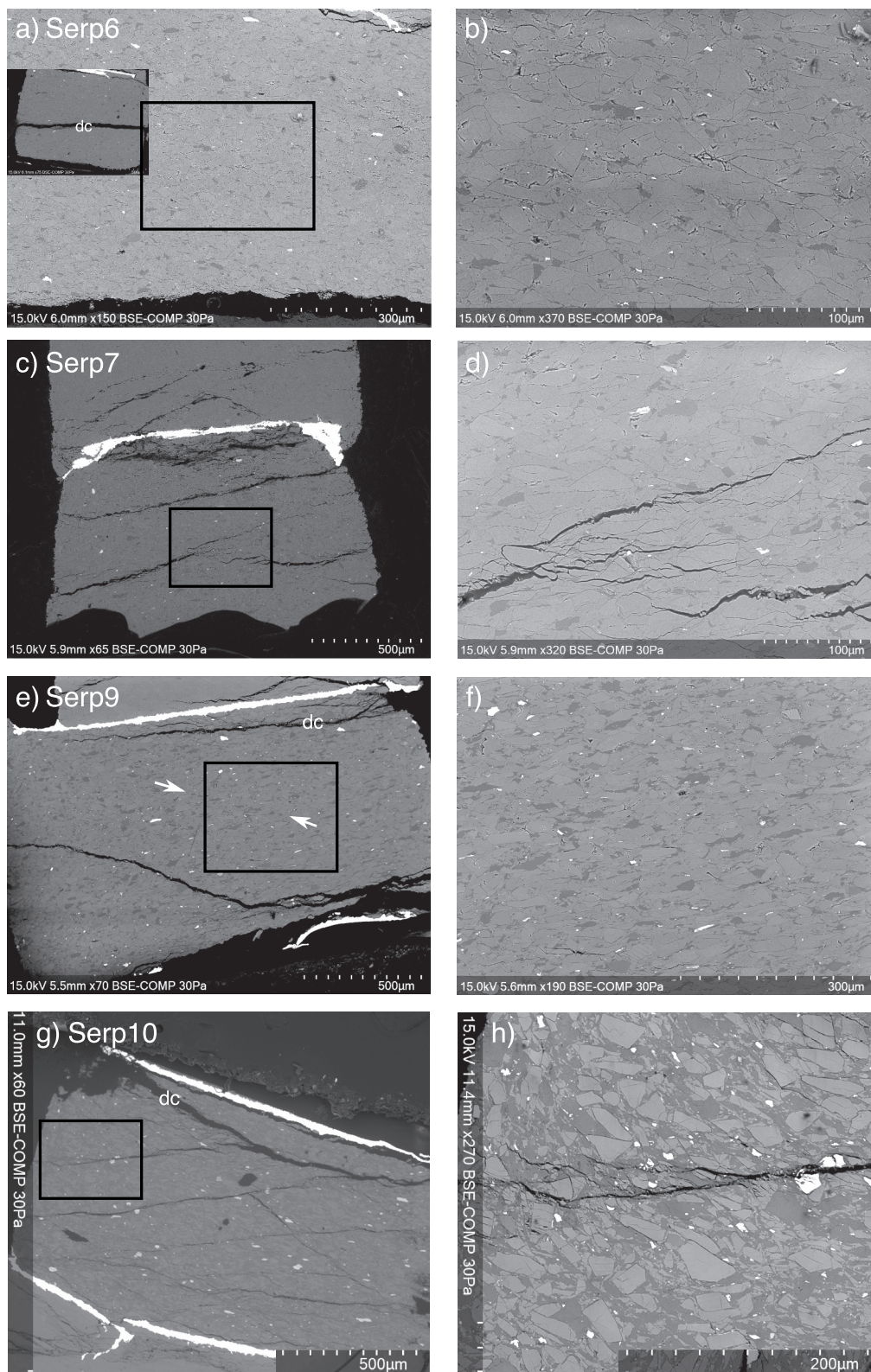


**Figure 3.** Electron microscopy (Back Scattered Electron) images of the recovered two-phase aggregates. The rectangles on the left column show the location of the smaller scale images on the right. Antigorite is dark gray on all images and olivine is light gray. The bright materials are the gold sheets used as strain markers, and iron oxides naturally present in the starting powders. The bottom of Serp7 in (c) is covered with conductive paste. dc = decompression crack. The white arrows in (e) show an en-echelon distribution of clusters, which may play a major role in obtaining a stress controlled by antigorite without having an interconnected network.

The EBSD data on olivine were analyzed using the Matlab MTEX toolbox (Bachmann et al., 2010). Figure 5 shows the pole figures in the two-phase aggregates compared with pole figures for their respective reference aggregate with 100% olivine (*Pbnm* setting).

The Crystal Preferred Orientations (CPO) on deformed samples are overall weak and are characterized by minima of [001] parallel to the maximum compression direction. The [100] axes define maxima slightly tilted from the maximum compression direction (or weak girdles around this direction). The [010] distribution relative to the maximum compression axis is more diffuse except on the *serp10* sample. All two-phase samples show maximum close to the compression direction.

To deconvolute the final CPO from the one resulting from the loading stage, the lattice preferred orientation (LPO) prior deformation have been analyzed for two-phase aggregates using their in situ X-ray diffractions, under high pressure and high temperature (see Figure S4 and Text in Supporting Information S1). Comparison with the starting textures shows that deformation induced, in all two-phase samples, rotation of *b* and *a* closer to the maximum compression direction.

In order to characterize the strength of the CPO we use the J-index (Bunge, 1982), which is 1 for a uniform distribution and infinite for a single orientation. The J-index for all samples is shown in Figure S5 in Supporting Information S1. Overall, the CPO intensity slightly increases with increasing total strain from 1.07 for the lowest strains to 1.22 for the highest antigorite fraction (50%) and large strain (−23.6%) in the two-phase aggregates. The reference olivine aggregates also show a trend with low J-index of 1.06, for the lowest strains (−12.9%), up to a J-index of 1.2 for the highest strains (−23.6%).

The crystal long axis orientations relative to the compression axis are shown on rose diagrams in Figure 5 for the two-phase and reference aggregates. This long axis is mostly oriented normal to the compression axis, which evidences a Shape Preferred Orientation (SPO).

The local misorientation within olivine grains gives information on the global strain gradient in the grain and the spatial distribution of this gradient. The Kernel Average Misorientation (KAM; angle, within a grain, between a pixel orientation and the mean orientation of its 4 neighbors) reveals local strain gradients within the grains while misorientations to the mean grain orientation (“Mis2Mean”) reflects the strain gradient at the grain scale. Maps of KAM and Mis2Mean highlight deformation styles of olivine that range between brittle to crystal-plastic end-members (Figure 6).

Crystals, especially large ones, show multiple intragranular microcracks, sometimes akin to cleavage. For some, deformation occurs mostly by microcracking and there is only limited misorientation relative to the mean grain orientation. In other cases, the crystals (small or large) show few or no microcracks and undulose to patchy orientation sectors developed within grains. For large grains, KAM maps also highlight a number of impingement microcracks, that is, crack radiating out of the contact sites with other grains (Passchier & Trouw, 2005). Grain microcracks tend to follow diagonal directions, and overall the deformation style is rather cataclastic. We also obtained inverse pole figures showing the rotation axis orientation for low-angle boundaries (2–10°) which are presented in Supporting Information S1 (Figure S6).

## 4. Discussion

### 4.1. Deformation Mechanisms

#### 4.1.1. Antigorite

The loss of definition of the antigorite peaks on the X-ray diffraction as deformation proceeded, especially on the 5 vol. % atg sample, can indicate one or all of the following processes in this sample: delamination, grain size reduction (comminution), loss of order in the layers stack, large scale crystal defects, and/or amorphization of antigorite crystals. These mechanisms, except for the stacking disorder, can create new weak zones and cause a decrease in measured stress. After about 18% strain, no peak could be seen anymore on the diffraction for the 5 vol. % atg sample.

We were unable to observe antigorite deformation mechanisms using EBSD. The difficulty in obtaining a signal suitable from EBSD was expected for the aggregates with low antigorite content, because the in situ XRD indicated some state akin to loss of crystal structure ordering or comminution. However, it was unexpected for the



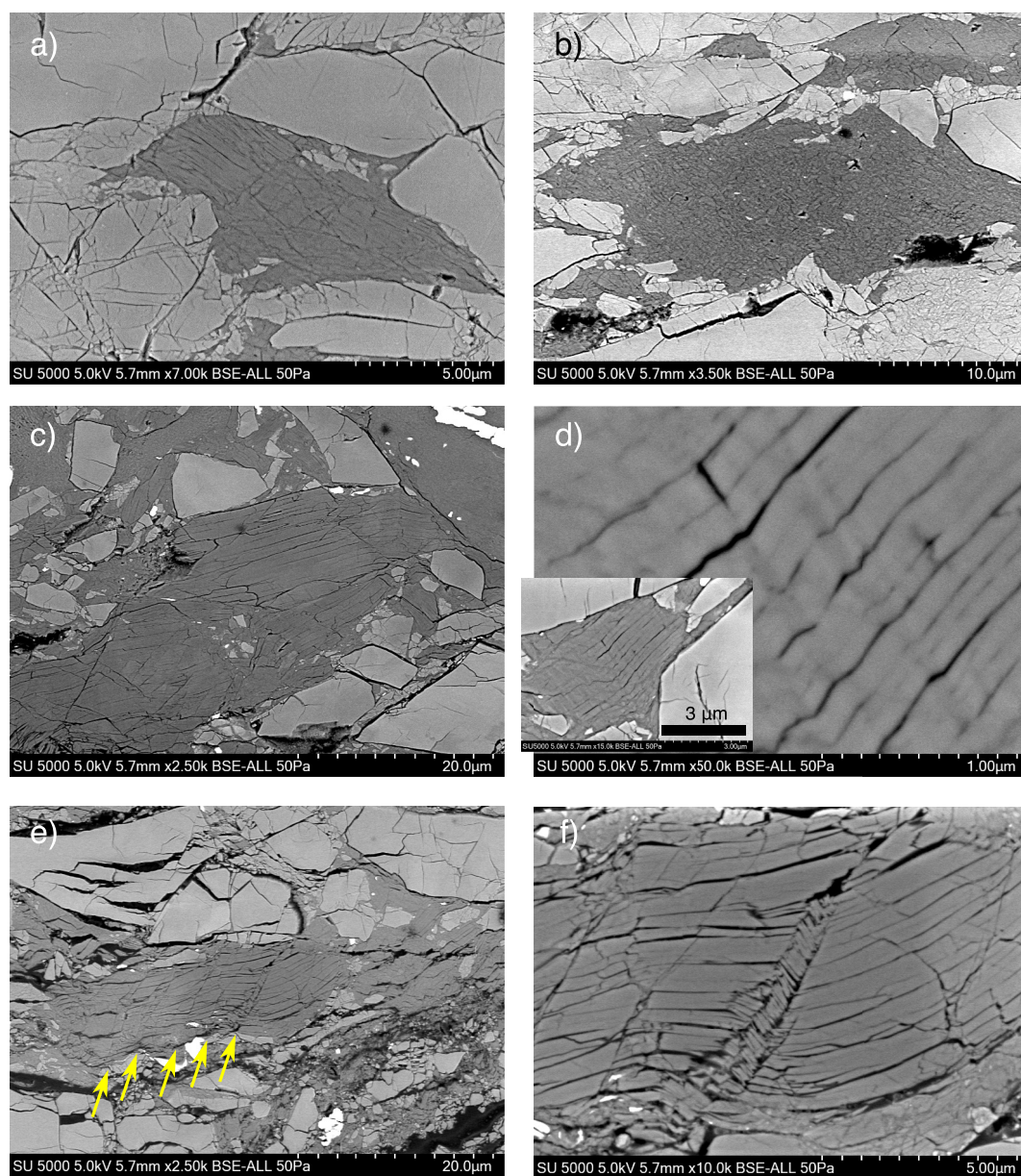


**Figure 4.** BSE images of deformation features in antigorite clusters, for 20% (a and b, serp9) and 50% (c, d, e, f, serp10) antigorite fraction samples. Antigorite is dark gray, olivine light gray and the bright phases are oxides. The maximum stress direction is vertical. In serp9: (a) antigorite crystal preserved with grain size reduction next to an olivine grain size reduction area and (b) intense grain size reduction area. In serp10: (c) large antigorite crystal preserved with an area of grain size reduction in the upper left part, (d) kink bands at the 100-nm scale in response to local strain field imposed by the olivine crystals (inset), (e) crystal deformed by a series of fractures and kinks with the same orientation (arrows) and bending, (f) close up of the kink-band with loss of cohesion between sheets. Further images for 5% and 10% vol. antigorite, see Figure S2 in Supporting Information S1.

aggregates with highest antigorite content. The small grain sizes lead to crystals being very easily scraped off the surface during preparation, which could have prevented obtaining a good enough polish on antigorite grains. Another possibility is a large number of defects or distortion in antigorite, too large for the crystals to provide an EBSD signal.

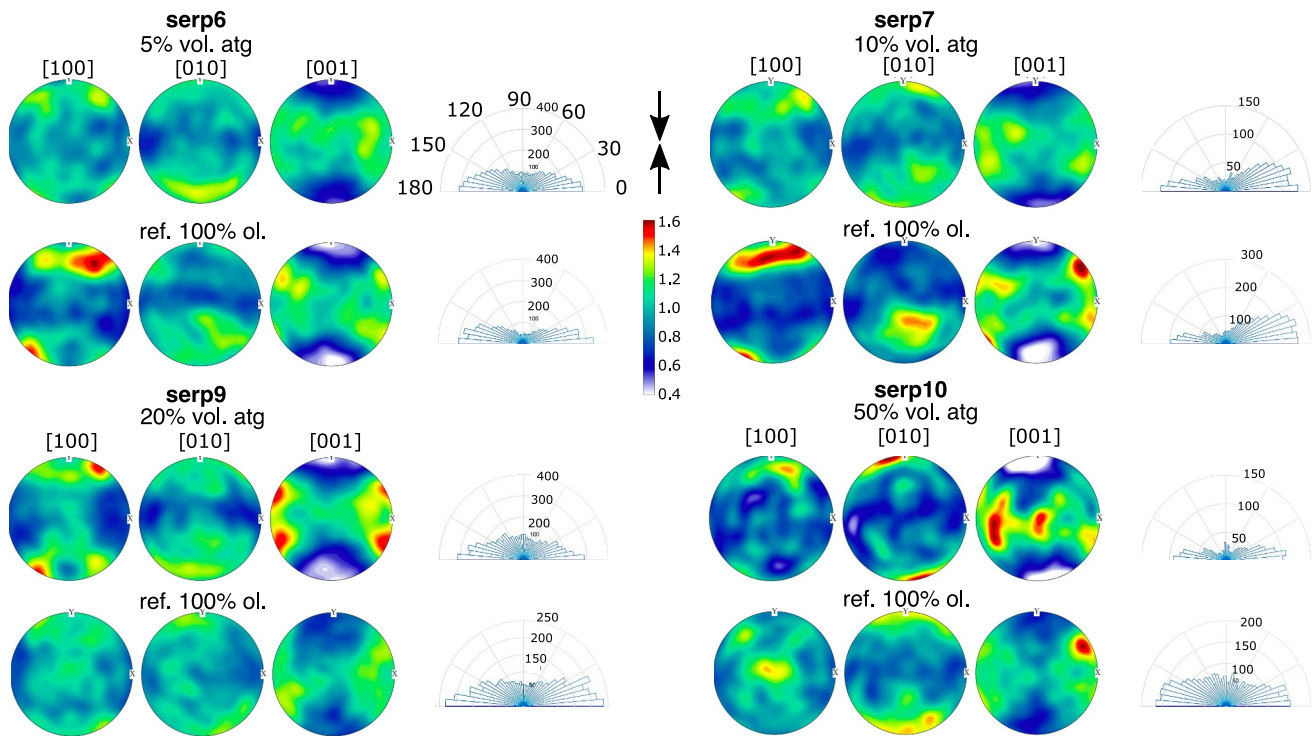


**Figure 5.** Olivine pole figures and grains long axis orientations in two-phase and reference aggregates, relative to the maximum compression direction, as obtained from EBSD on recovered samples. Color scale bar in mrd (multiples of random deviation); the maximum compression axis is vertical, indicated by the black arrows (90° on the rose diagrams).

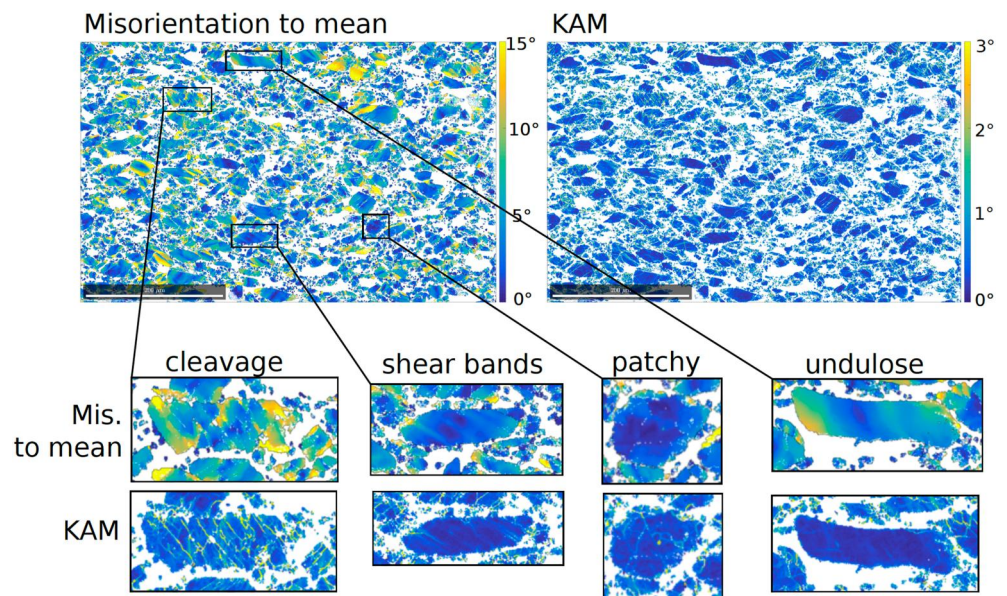


**Figure 6.** Misorientation to mean grain orientation and kernel average misorientation (KAM) maps on serp9 recovered two-phase aggregate (20 vol. % antigorite). Only olivine was analyzed; the white is serpentine and non-indexed regions. The different deformation styles of olivine crystals are highlighted. The scale bar on large maps is 200  $\mu\text{m}$ .

#### 4.1.2. Olivine

The analysis for the intracrystalline deformation mechanisms in olivine requires caution. The CPO are very weak, and the effect of dislocation glide is likely convoluted with crystal shape effects, that is, the SPO. The rose diagrams show a clear correlation between crystal shapes and orientations relative to the shortening axis, hence a well-defined SPO (Figure 5). For olivine reference aggregates (serp6 and 7, Table 1) the SPO is slightly stronger in the more deformed aggregates. This relationship is not clear for two-phase aggregates (Figure 5).

The CPO of reference aggregates in serp 6, serp7 and 20 vol. % atg aggregate in serp9 have a majority of [100] close to the maximum compression axis and a girdle of [001] perpendicular to the compression axis, which would be consistent with the (100)[001] slip system. The misorientation analysis Figure S6 in Supporting Information S1 gives further information about the dislocations locally accommodating the plastic deformation of olivine crystals, which are consistent with the suggested slip system.

We examined possible trends of deformation at the crystal scale with respect to the total sample strain, fraction of antigorite, and aggregate stress. Together with the KAM for local misorientation gradients, the grain orientation spread (GOS; average of Mis2Mean for each grain) was considered, which quantifies the global gradient of orientation existing in the grain. Statistics of the KAM and GOS are presented in Figure S7 in Supporting Information S1. The reference olivine aggregates tend to show increased median KAM and median GOS (Figure S7 in Supporting Information S1), that is, to be more damaged with increasing stress and strain. Meanwhile, in the olivine within the two-phase aggregates, the median GOS shows a slight tendency to decrease with antigorite fraction (or with decreasing stress) even at larger strains.

These observations are consistent with Wallis et al., 2011, who reported natural microstructures for antigorite free and antigorite bearing dunites of ca. 1 0%, 21% and 42% modal fraction of antigorite, derived from mantle wedge conditions in the Higashi-Akaishi body, NE Japan. They observed weakening of the olivine CPO with increasing antigorite fraction, due to phase boundary slip and rigid rotation of olivine grains.

#### 4.1.3. Deformation Mechanisms of the Aggregate

The SEM observations, CPO and SPO all point to (a) intracrystalline plasticity in olivine, which gradually generates the crystal lattice bending and undulose or patchy orientation domains in crystals, for accommodating local strain incompatibilities, and (b) a shortening mainly accommodated by crushing/cleaving of crystals, and by rigid rotation of olivine crystals according to their shape.

The rigid rotations imply grain boundary slip in olivine or between olivine and antigorite in a diffusionless sense (at this experimental timescale, because T is low and in the absence of fluid). Olivine crystal rotation can also be purely accommodated by strain in neighbouring antigorite, in the samples with higher antigorite fractions (e.g., serp10, Figure 3h).

The deformation style of antigorite clusters evolves with increasing antigorite fraction and is consistent with the stress analysis: the low stress in antigorite, for low antigorite fractions (serp6 and 7) is due to the olivine matrix controlling the strain. Hence, antigorite clusters in this case (Figures 3b and 3d) are weakly deformed. At 20 vol. % antigorite, the strain is no longer controlled by olivine only, and the antigorite clusters are sheared (Figure 3f). The antigorite clusters have maximum length scales around 200 microns and more typically are about 100 microns, and therefore are not connected in 2D over the aggregate length scale. We propose that the en-echelon organization of these clusters forms a weak zone in the aggregate at the scale of the group, even if the clusters are not connected. As proposed for instance by Gerbi et al. (2016), fine-grained olivine can form bridges between antigorite clusters and could also constitute weak zones (not obvious on our 2D images). More likely here, glide on bridging grain boundaries could also play a similar role.

The semi-brittle/brittle components of the aggregates' deformation in our experiments are further examined in the light of the available literature in Section 4.3.

#### 4.2. In Situ Stresses From X-Ray Data and Interpretation

Figure 7 compares the stresses within olivine and antigorite in the aggregates as a function of the serpentine fraction in the two-phase aggregate. The stress in the reference aggregate of each run is also reported.

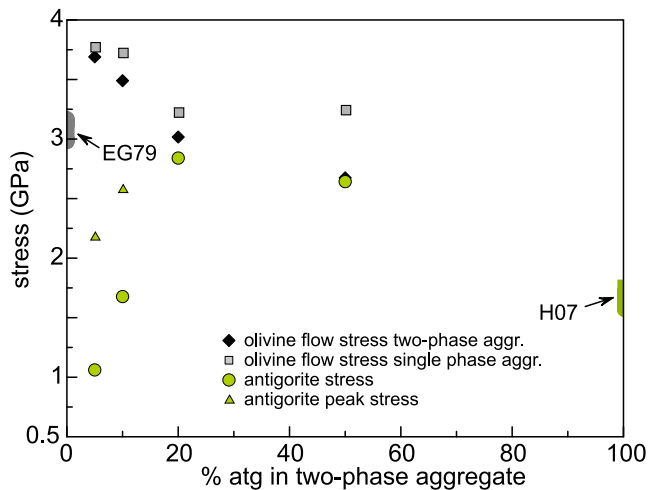


**Figure 7.** Stresses measured within olivine and antigorite in two-phase aggregates. The stresses for olivine (black) and for antigorite (green) are taken when the stresses have reached a « plateau » on the stress-strain curve (Table 1). For antigorite, the stress is measured only on the (001) plane, see discussion for its significance; the peak stress before the plateau, if any, is indicated by a light green triangle. Stresses in olivine reference aggregates (same run) are in gray. The range of expected stresses under the strain rate, T and P of the four experiments using flow laws by Evans and Goetze (1979) [EG79] and Hilairet et al. (2007) [H07] were calculated for single phase olivine and antigorite aggregates respectively. Note these experimental stresses are not normalized to same strain rate, pressure and temperature. Doing so has a modest effect on stress values and does not change the conclusions here.

Run serp9 showed macroscopic fracturing and a jump in strain for the olivine reference aggregate so comparison of its microstresses with the other runs presented here deserves to be justified. The stress curves in serp9 do not indicate a stress drop simultaneously with the strain jump. In previous works where high-pressure failure took place (e.g., Ferrand et al., 2017; Incel et al., 2017), the stress was measured on a small portion of the sample ( $200 \times 200 \mu\text{m}$  for a  $3 \times 2 \text{ mm}$  sample). In contrast, here the stress was measured on a larger sample area (ca.  $1 \text{ mm}$  wide  $\times$   $0.5 \text{ mm}$  height) centered over ca.  $1.3 \text{ mm}$  height aggregates, which means we were less likely to miss a major stress drop in the fractured region. We infer that fracturation is only evidenced in the strain data because the volume of crystals in which stress was « unloaded » by this fracturation remained small. Thus, we also consider the stress balance between the two phases in this experiment can be compared with our three other experiments.

In antigorite-poor aggregates (5 and 10 vol. %), the antigorite stress first increases above the stress expected for deformation of pure antigorite aggregates. The olivine framework imposes this transient overshoot in stress, since the overshoot is not observed in pure antigorite aggregates (e.g., Hilairet et al., 2007; Hirauchi et al., 2020). We postulate the antigorite is confined within the olivine matrix and first undergoes elastic compression leading to the peak in stress, because crystals are unable to deform freely (strain incompatibilities). After the transient, for 5 vol. % antigorite, the stress decreases below that expected for a pure antigorite aggregate. At that time, the stress in antigorite crystals could be shielded by olivine. Alternatively these low stresses could be due to deformation of very fine grained or partly amorphized antigorite. In the 10 vol. % antigorite aggregate, the stress given by antigorite after the transient stage is consistent with the flow stress expected for a pure antigorite aggregate. Thus the local strain rate imposed to the

antigorite patches may be close to that of the aggregate at this time. The deformation at the aggregate scale is buffered by the stress percolating within the framework of olivine crystals.

For the 20 and 50 vol. % antigorite aggregates, the stress balance is different from that with lower atg fraction. No transient regime is observed. Antigorite indicates higher stresses than expected from its flow law in these P, T and strain rate conditions, and similar to those of olivine (Figure 7). The explanation can reside in microstructural factors and/or come from different deformation mechanisms than those corresponding to the flow law in Hilairet et al. (2007). As for microstructural factors: with a weak CPO and five measured diffraction planes (which thus cover many different orientations in the olivine unit cell), the olivine stress is calculated from a population of diffracting grains that sample a large orientation range. The situation is quite different for serpentine, which becomes strongly textured in our experiments. The population of diffracting grains for the only measured diffraction plane (the basal plane (001)) is in vast majority made of grains oriented orthogonal to the beam when the stress plateau is reached. If deformation can occur in antigorite by a mechanism (as yet unclear), which end-result is glide more or less parallel to the (001) planes, most grains oriented perpendicular to the maximum stress direction are therefore not able to accommodate deformation anymore. Amiguet et al. (2012) investigated lizardite aggregate deformation, and referred to such population as having a « locked geometry ». Our lattice strain  $Q$  (001) is calculated from a full angular dispersive diffraction line, and therefore includes grains in « unlocked » orientations. However, the stronger the texture, the less unlocked grains can contribute, and the higher may become the influence of the locked grains on the stress as calculated from the lattice strains  $Q(hkl)$ . Thus, for our 20 and 50 vol. % antigorite samples, these locked grains are in an isostress state with the olivine crystals. The second factor that can explain this discrepancy is a mix of deformation mechanisms that are different than those occurring in Hilairet et al. (2007), specifically a larger part of brittle like mechanisms. This is examined in the next section.

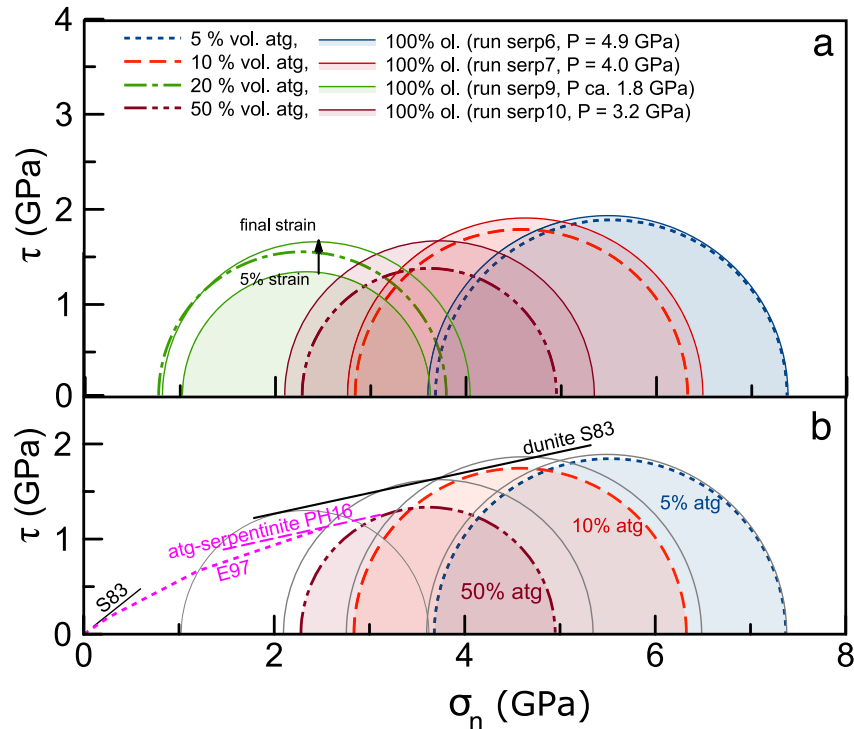


**Figure 8.** Strength of two-phase aggregates and comparison with friction laws for antigorite and olivine. (a) Mohr circles representing the stress state in two-phase and reference single-phase aggregates in this study, as calculated from in situ measurements of differential stress and pressure (mean stress). The stress values at final strain were considered as representative. For run serp9, stress state on the reference aggregate is plotted at ca. 5% (before strain jump; cf. Figure 1) and at final strain. (b) Data from this study compared with friction laws from literature: Escartin et al. (1997) [E97], Proctor and Hirth (2016) [PH16], for antigorite, and Shimada et al. (1983) [S83] for dunite. Serp9 two-phase aggregate stress state is not reported for clarity (in a), dashed green circle.

### 4.3. Comparison With Antigorite and Olivine Deformation Experiments From the Literature

In our experiments the deformation mechanisms are more akin to frictional processes *sensu lato* (diffusionless sliding on grain boundaries and cracks, microcracking and delamination) than purely (intra)crystalline defects-controlled processes, because of the high strain rates, low temperature, high stress level and the absence of fluids.

From X-ray diffraction, the “hydrostatic” pressure  $P$  (mean stress) and the differential stress  $\sigma_d$  are measured in situ. Taking compressive stresses as positive,  $\sigma_1$  and  $\sigma_3$  as the maximum and the minimum compressive stress respectively, assuming the transversal isotropy of stresses  $\sigma_2 = \sigma_3$  because of the cylindrical geometry of the sample and compression, we have  $P = \frac{1}{3}(\sigma_1 + 2\sigma_3)$  and  $\sigma_d = \sigma_1 - \sigma_3$ . Therefore  $\sigma_1$  and  $\sigma_3$  are straightforwardly obtained from  $\sigma_1 = P + \frac{2}{3}\sigma_d$  and  $\sigma_3 = P - \frac{1}{3}\sigma_d$ . From this, the state of stress on any given plane within the aggregate can be characterized and plotted as a Mohr circle.

The tangential stress  $\tau$  on a plane reads:

$$\tau = \frac{1}{2}\sigma_d \sin 2\alpha$$

where  $\alpha$  is the angle between the plane normal and the minimum compressive stress ( $\alpha$  is used to avoid confusion with  $\theta$  already defined as the diffraction angle).

The normal stress  $\sigma_n$  reads:

$$\sigma_n = \left(\frac{\sigma_1 + \sigma_3}{2}\right) - \left(\frac{\sigma_1 - \sigma_3}{2}\right) \cos 2\alpha.$$

Figure 8a shows this stress state as Mohr-Coulomb circles for pure olivine and two-phase aggregates in this study. For the run serp10, the stress state actually used for the figure in the reference aggregate is taken at 13% shortening, while for the two-phase aggregate the total strain is above 20%. Since in the latter, the stress does not vary between 13% and 20% strain (Figure 2 lower right) they can still be compared here. For the same reason, the stress states of the other runs are also those at the final strain even if these differ (Table 1).

In Figure 8b, we compare these data with friction laws and fracture envelopes from the literature, that is, the so-called Byerlee law defined by a compilation of rock mechanical data (friction) up to 2 GPa for  $\sigma_n$  (Byerlee, 1978), and the fracture envelope reported for the Horoman dunite by Shimada et al. (1983). The results on olivine aggregates by Boettcher et al. (2007) are not included because less relevant (with fluid, up to 300 MPa effective pressure only, and temperatures from 600°C to 1000°C). For antigorite aggregates, the Mohr envelope obtained by Escartin et al. (1997) and Proctor and Hirth (2016) at higher pressures are shown.

For reference aggregates (100% olivine) in serp6, serp7 and serp10, the stress states on Figure 8 do correspond to the fracture envelope determined on the Horoman dunite by Shimada et al. (1983). For the two-phase aggregates, when antigorite fraction is low (5 vol. % atg), the olivine indicates a state of stress similar to the pure olivine aggregate. Meanwhile, for high antigorite content (50 vol. %), the stress state in olivine is much lower than in the reference, and can be interpreted as buffered by the antigorite frictional properties measured by Escartin et al. (1997) and Proctor and Hirth (2016). In this case, olivine crystals likely behave as rigid inclusions. Antigorite indeed controls the deformation above 20 vol. % antigorite, and mechanisms akin to frictional processes, such as those reported at lower pressure, control the stress in antigorite.

In run serp9 the state of stress in the reference aggregate at the final strain is above the envelope defined by Shimada et al. (1983). When the stress state is taken at 5% strain, where a strain jump occurs (Figure 1) likely due to a sample fracture, the Mohr circle actually fits the fracture envelope (Figure 8, circle marked 5% strain). Further increase in stress may be an indication of the fracture being locked and/or of sample hardening due to intracrystalline defect multiplication. For the antigorite + olivine aggregate in this run the stress state is also well above the fracture envelope for dunite, and the friction law defined for pure antigorite aggregates in Proctor and Hirth (2016) (similar to its reference olivine aggregate). The stress state is however, in this run, measured from the olivine crystals and a subpopulation of antigorite crystals in locked orientations. The actual stress under which the two-phase aggregate deforms (i.e., force over surface), may be lower than the one measured in these olivine and antigorite crystals, in the case of deformation localization. The en-echelon organization seen in Figure 3e is a candidate region in this sample. Hardening may be invoked in other regions of the sample.

Note that Shimada's experiments had a larger grain size (0.1–0.9 mm compared to 1–40 microns here) and were conducted at ambient T, while our experiments are at 300–350°C. Therefore the dependence of fracturation/frictional properties of olivine on grain size or T of aggregates cannot be discussed here. We also provide in Figure S8 in Supporting Information S1 a comparison with data available for deformation of olivine or antigorite under low T at similar or higher confining pressures that plot close to or above the Goetze criterion, together with a short discussion.

In summary, our data at low temperature are consistent with previously determined friction laws in olivine and antigorite aggregates, and suggest their continuity for T up to ca 350°C, even at these high pressures up to 4–5 GPa. Experiments under low temperature below ca. 900 K, and high pressures above ca. 2 GPa, are commonly fitted using an exponential flow law—which implies a deformation controlled by dislocation glide under high stresses. It is yet unclear to us whether one of these frameworks represents best our data. This calls for a better understanding of how to describe deformation mechanisms within antigorite aggregates, which do not obey simple dislocation glide-based mechanisms (Hansen et al., 2020; Idrissi et al., 2020).

#### 4.4. Antigorite Fraction: Threshold for Changes in Mechanical Control

The differences in strain rates and in situ stresses recorded by the 5 and 10 vol. % antigorite aggregates on one side, and the 20 and 50 vol. % antigorite aggregates on the other side, highlight a change in the aggregate mechanical behavior between 10 and 20 vol. % antigorite. This value is also reflected in the change in local olivine crystal plasticity as previously discussed (see olivine deformation mechanisms, Section 4.1.2). This threshold does correspond to the usual values for stress percolation problems of a weak phase within the framework of a stronger phase (e.g., Karato, 2008).

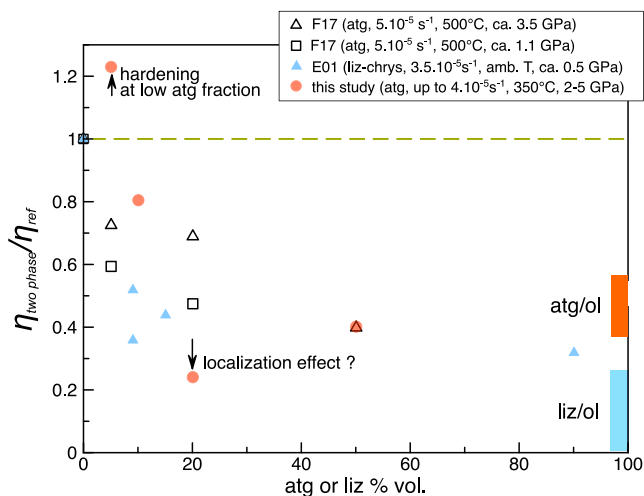


**Figure 9.** Contrast in  $\eta = \frac{\sigma}{\dot{\epsilon}}$  between serpentine + olivine aggregates and pure olivine aggregates, from this study and the literature. The aggregate strengths in this study are normalized by the strain rates (all different from one aggregate to another), the two phase aggregates compared against the reference aggregate for each run. Data from Ferrand et al., 2017 (F17) were normalized using their 100% olivine aggregates runs at 3.5 and 1.1 GPa. Lizardite-serpentinites data from Escartin et al., 2001 (E01) were normalized using their unaltered Horoman Dunite data with the pressure (mean stress) calculated from the confining pressure ( $\sigma_3$ ) and the differential stress. The contrast for antigorite or lizardite rocks compared to dunite ([atg/ol] and [liz/ol] respectively) is calculated from published flow laws which implies theoretically deformation controlled by dislocation motion processes. Hilairet et al. (2007) is used for antigorite, Amiguet et al. (2012) for lizardite, and Evans and Goetze (1979) for olivine with strain rate  $2.10^{-5}\ s^{-1}$ , P between 1 and 3 GPa, T at  $400^{\circ}C$ . See Sections 4.4 and 4.5 for discussion.

Goetze (1979) using an indentation technique. Those at lower pressures are consistent with Evans and Goetze (1979). The higher stresses seen in the highest pressure experiments thus could be due to the pressure effect on the deformation mechanisms, not taken into account in the flow law by Evans and Goetze (1979).

In addition to these pressures differences, the strain rates at which the single-phase aggregates and two-phase aggregates deform here differ, up to a factor of almost 4. We attempt here to make a comparison “free” from strain rate and pressures variations by defining for the two-phase and reference aggregates in each experiment:

$$\eta_{two\ phase} = \frac{\sigma_{two\ phase}}{\dot{\epsilon}_{two\ phase}} \text{ and } \eta_{ref} = \frac{\sigma_{ref}}{\dot{\epsilon}_{ref}}$$

Figure 9 shows the evolution of the ratio  $\frac{\eta_{two\ phase}}{\eta_{ref}}$  as a function of antigorite content, and a comparison with literature data. Studies at higher temperatures are not included for the sake of clarity, but can be found in Ferrand (2017). Contrasts expected for monomineralic antigorite or lizardite (chrysotile) rocks with respect to dunite, are calculated from published flow laws (Amiguet et al., 2012; Evans & Goetze, 1979; Hilairet et al., 2007). The flow laws calculated contrasts are consistent with the shear strain contrasts between pure antigorite, lizardite (chrysotile) and olivine aggregates found by Hirauchi and Katayama (2013) at  $300^{\circ}C$  under 1 GPa confining pressure. Note the use of these flow laws for pure end members implies a deformation by dislocation-motion controlled processes, while our data seem (also) consistent with friction-like controlled behavior.

At moderate temperatures, our aggregate with 5 vol. % antigorite has a higher  $\frac{\sigma}{\dot{\epsilon}}$  than its single-phase counterpart in the same run, with similar stresses in both aggregates. The lower strain rate of the two-phase aggregate is what causes this apparent higher “viscosity,” and could be interpreted as a result of local hardening of olivine at low serpentine fractions. Handy (1990) for instance (his Figure 1) suggest a hardening effect at low amounts of weak phase in such aggregates. Comparing with Ferrand et al. (2017), we infer this hardening vanishes closer to

This threshold is somewhat different from that obtained in experiments at ambient T by Escartin et al. (2001) in which about 5–10 vol. % lizardite and chrysotile serpentine decreased the overall strength of serpentized peridotites by a factor of 2–3. This difference is easily explained by the crystallographic structure of antigorite (e.g., Amiguet et al., 2012; Escartin et al., 2001) which is more compact than lizardite. As a result, lizardite (and chrysotile) have internal friction coefficients much lower than antigorite (Escartin et al., 1997). A second explanation resides in the microstructure: while our samples are synthetic aggregates with patches or grains of antigorite within a matrix of olivine, the rock used by Escartin et al. (2001) was a peridotite in which former olivine grain boundaries were lined up by lizardite and chrysotile, interconnected despite a low volume content. As proposed by Handy (1990), this comparison illustrates that microstructure is crucial in controlling and modifying the mechanical behavior of an aggregate even at modest strains.

Ferrand et al. (2017) and Ferrand (2017) used the same starting material than in this study, with varying antigorite contents (0, 5, 20 and 50 vol. %) for investigation of the link between intermediate-depth earthquakes and serpentine dehydration, in similar conditions of strain, pressure, similar microstructure, and higher temperature (ca.  $500^{\circ}C$ ) and strain rates ( $5.10^{-5}$  to  $10^{-4}\ s^{-1}$ ). In Ferrand et al. (2017), aggregates containing as little as 5 vol. % antigorite showed already lower olivine stresses than pure olivine aggregates in the same conditions, suggesting that temperature or strain rate modify the elastic and crystal-plastic interactions between olivine and antigorite.

Given the microstructural observations, the single-crystal strength of olivine is expected to have a major role in controlling deformation of the reference aggregates or antigorite-poor aggregates. However, the stresses obtained for the 100% olivine reference aggregate and two-phase aggregates at the highest pressures, are higher than single-crystal hardness measured by Evans and

dehydration temperatures because intracrystalline deformation processes are more active. Figure 9 is further discussed in the next section.

#### 4.5. Applicability to Subduction Zone Dynamics

Our aggregates with varied antigorite contents can be considered as a proxy for dunite with different serpentinization degrees, and our olivine aggregates as a proxy for a mantle unaltered dunite. Figure 9 thus shows estimates of the strength or viscosity contrast between these two rocks at our experimental strain rates, that is, for timescales ranging from hours to days.

At high pressures corresponding to depths of 90 km, our results suggest the viscosity could be inverted at very low serpentine (5%) fractions because of the local concentration of stresses. The viscosity contrast could remain on the order of 0.7 or higher for a serpentine amount of 10 vol. %, and around 0.4 to 0.5 for 50% serpentinization or more. The viscosity contrast for 20 vol. % antigorite, lower than 0.3, may be due to the proposed strain localization along the en-echelon antigorite clusters. Further experiments would be needed to clarify the role of mean stress here.

The viscosity contrast becomes larger for a lower serpentine amount, in the lower pressure, higher temperature series in the antigorite-bearing samples in Ferrand et al. (2017, 1.1 GPa series), and for the lizardite-chrysotile serpentinites deformed under a mean stress ca. 0.5 GPa and at ambient T in Escartin et al. (2001). The difference between our results and those of Ferrand et al. (2017) at low antigorite contents, is likely the balance of controlling deformation mechanisms for olivine. Frictional processes *s.l.* occur in our experiments at low T, while intracrystalline olivine plasticity can be expected more active at higher T (e.g., results by Raterron et al., 2004). This may however be mitigated by an increased strain rate.

For a large serpentine content (50% and more) at first order the strength contrast between a serpentinized rock and an olivine rock does not seem to depend on the T or the mix in deformation mechanisms (brittle-like vs. intracrystalline): this contrast is similar and around 0.4 to 0.5, whether it is taken at high T (Ferrand et al., 2017), in our aggregates at lower T, or if calculated from a flow law in a pure antigorite rock with a different mix of these deformation mechanisms.

The hardening of the aggregate with the lowest serpentine fraction (5%) relative to pure olivine aggregate, and the shielding of stress within antigorite for 5 and 10 vol. % serpentine aggregates, can be related to the creation of load-bearing networks (e.g., Handy, 1990, 1994) or force chains (a concept widely known in granular mechanics, e.g. Peters et al., 2005) through the harder olivine grains, in contact with each other. The relevance of this hardening for a natural serpentinized peridotite and for different microstructures remains to be demonstrated. Recently, Burnley (2013), and Beall et al. (2019a, 2019b), studied numerically the development of force chains in deforming aggregates, and shear zones at cm to m scale, respectively. These studies, the results by Ferrand et al. (2017) on dehydrating antigorite + olivine aggregates, Ferrand (2019), and the present study, suggest that when the weak component is between 0 and 20 vol. %, understanding the modalities of load-bearing networks appearance, and characterizing them at several scales, is essential in describing the rheology of polymineralic and matrix/clast mélanges.

Our data set remains limited, with several parameters at play that have opposite effects (temperature, pressure, strain rate, plastic properties of crystals, and microstructure). Extrapolation to the natural context and background strain rates must be made with caution. First, the displacement and stress geometry on shear zones, and the resulting microstructure, may be best represented by simple shear experiments. Lower strain rates may lead to different plastic relaxation interactions between antigorite and olivine. Fluids circulate at least episodically in shear zones, in subduction settings, and these fluids promote very different deformation mechanisms in serpentinites such as pressure solution (e.g., Auzende et al., 2015), especially when considering long timescales.

The results here, nonetheless, provide clues on the stress distribution in, and strength contrasts between, rocks when subject to relatively high stresses and high strain rates which may arise in subduction zones. They could be relevant to ductile deformation of serpentinized zones (or shear zones reactivation) upon stress transfer from loaded parts of the subduction zones (e.g., models by Montési & Hirth, 2003, Regenauer-Lieb & Yuen, 2008, Montési, 2013, Goswami & Barbot, 2018, observations by Hirauchi et al., 2021), where high stresses/fast strain rates may transiently be achieved, and to events that occur on timescales of hours to days, such as slow slip events. Since they are carried out under high pressures (>GPa) and at a temperature close to 350°C, our results could be particularly relevant for the rheology of the so-called stable sliding zone of the interface between the slab and



mantle, for the transition between stable sliding and seismic zones, and for understanding the stress state(s) within cold subducting slabs.

## Data Availability Statement

The stress and strain data from this study are available as .tab files, in Hilaret et al. (2024) in the Recherche Data Gouv repository.

## Acknowledgments

We thank Ken-ichi Hirauchi, an anonymous reviewer and the Associate Editor for their comments that helped improve a previous version of this manuscript, and Keishi Okazaki and Sando Sawa for their reviews. The experiments were performed on the ID06-LVP beamline at the European Synchrotron Radiation Facility (ESRF), Grenoble, France. The EBSD part of the electron microscopy was performed at the EBSD facility at Geosciences Montpellier, a national facility of CNRS-INSU (Institut National pour les Sciences de l'Univers). The remaining SEM images were obtained at the PMEL facility in Lille (France), supported by the Conseil Régional Hauts-de-France, and the European Regional Development Fund (ERDF). We thank F. Barou and C. Nevado (U. Montpellier) for assistance with the EBSD measurements and samples polishing. N.H. and S.M. acknowledge the Institut Chevreul for help in the development of this work (facility funding) through the ARCHI-CM project supported by the "Ministère de l'Enseignement Supérieur de la Recherche et de l'Innovation" the region "Hauts-de-France" the ERDF program of the European Union and the "Métropole Européenne de Lille". T. P. F. was supported by the ANR projet DELF to A. Schubnel (ANR12-JS06-0003) early in this work, and by the Alexander von Humboldt Foundation (TPF grant). P. R. research activities were in part carried out while P. R. was serving at the National Science Foundation (NSF). This study was initiated thanks to the financial support of the INSU Programme National de Planétologie to N.H. and P.R., and funded by the Agence Nationale pour la Recherche (MADISON, ANR-17-CE31-0012-01 to N.H.).

## References

- Abers, G. A., Nakajima, J., van Keken, P. E., Kita, S., & Hacker, B. R. (2013). Thermal-petrological controls on the location of earthquakes within subducting plates. *Earth and Planetary Science Letters*, 369, 178–187. <https://doi.org/10.1016/j.epsl.2013.03.022>
- Abers, G. A., van Keken, P. E., Kneller, E. A., Ferris, A., & Stachnik, J. C. (2006). The thermal structure of subduction zones constrained by seismic imaging: Implications for slab dehydration and wedge flow. *Earth and Planetary Science Letters*, 241(3–4), 387–397. <https://doi.org/10.1016/j.epsl.2005.11.055>
- Agard, P., Plunder, A., Angiboust, S., Bonnet, G., & Ruh, J. (2018). The subduction plate interface: Rock record and mechanical coupling (from long to short timescales). *Lithos*, 320, 537–566. <https://doi.org/10.1016/j.lithos.2018.09.029>
- Amiguet, E., Reynard, B., Caracas, R., Van de Moortele, B., Hilaret, N., & Wang, Y. B. (2012). Creep of phyllosilicates at the onset of plate tectonics. *Earth and Planetary Science Letters*, 345, 142–150. <https://doi.org/10.1016/j.epsl.2012.06.033>
- Auzende, A. L., Escartin, J., Walte, N. P., Guillot, S., Hirth, G., & Frost, D. J. (2015). Deformation mechanisms of antigorite serpentinite at subduction zone conditions determined from experimentally and naturally deformed rocks. *Earth and Planetary Science Letters*, 411, 229–240. <https://doi.org/10.1016/j.epsl.2014.11.053>
- Bachmann, F., Hielscher, R., & Schaeben, H. (2010). Texture analysis with MTEX - Free and open source software toolbox. In H. Klein & R. A. Schwarzer (Eds.), *Texture and anisotropy of polycrystals III*. <https://doi.org/10.4028/www.scientific.net/SSP.160.63>
- Beall, A., Fagereng, A., & Ellis, S. (2019a). Fracture and weakening of jammed subduction shear zones, leading to the generation of slow slip events. *Geochemistry, Geophysics, Geosystems*, 20(11), 4869–4884. <https://doi.org/10.1029/2019GC008481>
- Beall, A., Fagereng, A., & Ellis, S. (2019b). Strength of strained two-phase mixtures: Application to rapid creep and stress amplification in subduction zone mélange. *Geophysical Research Letters*, 46(1), 169–178. <https://doi.org/10.1029/2018GL081252>
- Bezacier, L., Reynard, B., Bass, J. D., Sanchez-Valle, C., & Van de Moortele, B. (2010). Elasticity of antigorite, seismic detection of serpentinites, and anisotropy in subduction zones. *Earth and Planetary Science Letters*, 289(1–2), 198–208. <https://doi.org/10.1016/j.epsl.2009.11.009>
- Boettcher, M. S., Hirth, G., & Evans, B. (2007). Olivine friction at the base of oceanic seismogenic zones. *Journal of Geophysical Research: Solid Earth*, 112(B1), B01205. <https://doi.org/10.1029/2006jb004301>
- Bunge, H. J. (1982). Texture analysis in material sciences: Mathematical methods.
- Burdette, E., & Hirth, G. (2022). Creep rheology of Antigorite: Experiments at subduction zone conditions. *Journal of Geophysical Research: Solid Earth*, 127(7), e2022JB024260. <https://doi.org/10.1029/2022JB024260>
- Burnley, P. C. (2013). The importance of stress percolation patterns in rocks and other polycrystalline materials. *Nature Communications*, 4(1), 2117. <https://doi.org/10.1038/ncomms3117>
- Burnley, P. C. (2015). Elastic plastic self-consistent (EPSC) modeling of plastic deformation in fayalite olivine. *American Mineralogist*, 100(7), 1424–1433. <https://doi.org/10.2138/am-2015-5234CCBYNCND>
- Burnley, P. C., & Zhang, D. (2008). Interpreting in situ x-ray diffraction data from high pressure deformation experiments using elastic-plastic self-consistent models: An example using quartz. *Journal of Physics: Condensed Matter*, 20(28), 285201. <https://doi.org/10.1088/0953-8984/20/28/285201>
- Byerlee, J. (1978). Friction of rocks. *Pure and Applied Geophysics*, 116(4–5), 615–626. <https://doi.org/10.1007/BF00876528>
- Canova, G. R., Wenk, H. R., & Molinari, A. (1992). Deformation modeling of multiphase polycrystals - Case of a quartz mica aggregate. *Acta Metallurgica et Materialia*, 40(7), 1519–1530. [https://doi.org/10.1016/0956-7151\(92\)90095-v](https://doi.org/10.1016/0956-7151(92)90095-v)
- Chen, J. H., Li, L., Yu, T., Long, H. B., Weidner, D., Wang, L. P., & Vaughan, M. (2006). Do Reuss and Voigt bounds really bound in high-pressure rheology experiments? *Journal of Physics: Condensed Matter*, 18(25), S1049–S1059. <https://doi.org/10.1088/0953-8984/18/25/s11>
- Chernak, L. J., & Hirth, G. (2010). Deformation of antigorite serpentinite at high temperature and pressure. *Earth and Planetary Science Letters*, 296(1–2), 23–33. <https://doi.org/10.1016/j.epsl.2010.04.035>
- Chernak, L. J., & Hirth, G. (2011). Syndeformational antigorite dehydration produces stable fault slip. *Geology*, 39(9), 847–850. <https://doi.org/10.1130/G31919.1>
- Cook, A. C., Vel, S. S., Gerbi, C., & Johnson, S. E. (2014). Computational analysis of nonlinear creep of polyphase aggregates: Influence of phase morphology. *Journal of Geophysical Research: Solid Earth*, 119(9), 6877–6906. <https://doi.org/10.1002/2014JB011197>
- Cyprich, D., Brune, S., Piazzolo, S., & Quinteros, J. (2016). Strain localization in polycrystalline material with second phase particles: Numerical modeling with application to ice mixtures. *Geochemistry, Geophysics, Geosystems*, 17(9), 3608–3628. <https://doi.org/10.1002/2016gc006471>
- Dobson, D. P., Meredith, P. G., & Boon, S. A. (2002). Simulation of subduction zone seismicity by dehydration of serpentine. *Science*, 298(5597), 1407–1410. <https://doi.org/10.1126/science.1075390>
- Druiventak, A., Trepmann, C. A., Renner, J., & Hanke, K. (2011). Low-temperature plasticity of olivine during high stress deformation of peridotite at lithospheric conditions—An experimental study. *Earth and Planetary Science Letters*, 311(3–4), 199–211. <https://doi.org/10.1016/j.epsl.2011.09.022>
- Escartin, J., Hirth, G., & Evans, B. (1997). Nondilatant brittle deformation of serpentinites: Implications for Mohr-Coulomb theory and the strength of faults. *Journal of Geophysical Research: Solid Earth*, 102(B2), 2897–2913. <https://doi.org/10.1029/96jb02792>
- Escartin, J., Hirth, G., & Evans, B. (2001). Strength of slightly serpentinitized peridotites: Implications for the tectonics of oceanic lithosphere. *Geology*, 29(11), 1023–1026. <https://doi.org/10.1130/0091-7613>
- Evans, B., & Goetze, C. (1979). Temperature variation of hardness of olivine and its implication for polycrystalline yield stress. *Journal of Geophysical Research*, 84(B10), 5505–5524. <https://doi.org/10.1029/JB084iB10p05505>
- Evans, B. W. (2004). The serpentinite multsystem revisited: Chrysotile is metastable. *International Geology Review*, 46(6), 479–506. <https://doi.org/10.2747/0020-6814.46.6.479>

- Farla, R., Rosenthal, A., Bollinger, C., Petitgirard, S., Guignard, J., Miyajima, N., et al. (2017). High-pressure, high-temperature deformation of dunite, eclogite, clinopyroxenite and garnetite using in situ X-ray diffraction. *Earth and Planetary Science Letters*, 473, 291–302. <https://doi.org/10.1016/j.epsl.2017.06.019>
- Federico, L., Crispini, L., Scambelluri, M., & Capponi, G. (2007). Ophiolite mélange zone records exhumation in a fossil subduction channel. *Geology*, 35(6), 499–502. <https://doi.org/10.1130/G23190A.1>
- Ferrand, T. P. (2017). *Reproduction expérimentale d'analogues de séismes mantelliques par déshydratation de l'antigorite & Comparaison à des pseudotachylites naturelles (doctoral dissertation)* PSL Research University. Retrieved from <https://tel.archives-ouvertes.fr/tel-01559226>
- Ferrand, T. P. (2019). Seismicity and mineral destabilizations in the subducting mantle up to 6 GPa, 200 km depth. *Lithos*, 334, 205–230. <https://doi.org/10.1016/j.lithos.2019.03.014>
- Ferrand, T. P., Hilaret, N., Incel, S., Deldicque, D., Labrousse, L., Gasc, J., et al. (2017). Dehydration-driven stress transfer triggers intermediate-depth earthquakes. *Nature Communications*, 8(1), 15247. <https://doi.org/10.1038/ncomms15247>
- Gaboriaud, R. J., Darot, M., Gueguen, Y., & Woignard, J. (1981). Dislocations in olivine indented at low temperatures. *Physics and Chemistry of Minerals*, 7(2), 100–104. <https://doi.org/10.1007/bf00309460>
- Gasc, J., Hilaret, N., Yu, T., Ferrand, T., Schubnel, A., & Wang, Y. (2017). Faulting of natural serpentinite: Implications for intermediate-depth seismicity. *Earth and Planetary Science Letters*, 474, 138–147. <https://doi.org/10.1016/j.epsl.2017.06.016>
- Gasc, J., Schubnel, A., Brunet, F., Guillon, S., Mueller, H.-J., & Lathe, C. (2011). Simultaneous acoustic emissions monitoring and synchrotron x-ray diffraction at high pressure and temperature: Calibration and application to serpentinite dehydration. *Physics of the Earth and Planetary Interiors*, 198(3–4), 121–133. <https://doi.org/10.1016/j.pepi.2011.08.003>
- Gerbi, C., Johnson, S. E., Shulman, D., & Klepeis, K. (2016). Influence of microscale weak zones on bulk strength. *Geochemistry, Geophysics, Geosystems*, 17(10), 4064–4077. <https://doi.org/10.1002/2016GC006551>
- Girard, J., Amulele, G., Farla, R., Mohiuddin, A., & Karato, S.-i. (2016). Shear deformation of bridgmanite and magnesio-wüstite aggregates at lower mantle conditions. *Science*, 351(6269), 144–147. <https://doi.org/10.1126/science.1231131>
- Goswami, A., & Barbot, S. (2018). Slow-slip events in semi-brittle serpentinite fault zones. *Scientific Reports*, 8(1), 6181. <https://doi.org/10.1038/s41598-018-24637-z>
- Guignard, J., & Crichton, W. A. (2015). The large volume press facility at ID06 beamline of the European synchrotron radiation facility as a high pressure-high temperature deformation apparatus. *Review of Scientific Instruments*, 86(8). <https://doi.org/10.1063/1.4928151>
- Guillot, S., Schwartz, S., Reynard, B., Agard, P., & Prigent, C. (2015). Tectonic significance of serpentinites. *Tectonophysics*, 646, 1–19. <https://doi.org/10.1016/j.tecto.2015.01.020>
- Guyot, F., Wang, Y. B., Gillet, P., & Ricard, Y. (1996). Quasi-harmonic computations of thermodynamic parameters of olivines at high-pressure and high-temperature. A comparison with experiment data. *Physics of the Earth and Planetary Interiors*, 98(1–2), 17–29. [https://doi.org/10.1016/S0031-9201\(96\)03174-3](https://doi.org/10.1016/S0031-9201(96)03174-3)
- Hammersley, A. P. (2016). FIT2D: A multi-purpose data reduction, analysis and visualization program. *Journal of Applied Crystallography*, 49(2), 646–652. <https://doi.org/10.1107/s1600576716000455>
- Handy, M. R. (1990). The solid-state flow of polyminerals rocks. *Journal of Geophysical Research-Solid Earth and Planets*, 95(B6), 8647–8661. <https://doi.org/10.1029/JB095iB06p08647>
- Handy, M. R. (1994). Flow laws for rocks containing 2 non-linear viscous phases - A phenomenological approach. *Journal of Structural Geology*, 16, 1727. <https://doi.org/10.1029/JB095iB06p08647>
- Hansen, L. N., David, E. C., Brantut, N., & Wallis, D. (2020). Insight into the microphysics of antigorite deformation from spherical nano-indentation. *Philosophical Transactions of the Royal Society A: Mathematical, Physical & Engineering Sciences*, 378(2165), 20190197. <https://doi.org/10.1098/rsta.2019.0197>
- Hilaret, N., Guignard, J., Ferrand, T. P., Merkel, S., Raterron, P., & Crichton, W. (2024). In situ strain and stresses in two phase olivine+antigorite aggregates deformed at subduction zones pressures (version 1) [Dataset]. *Recherche Data Gov.* <https://doi.org/10.57745/ZCHKER>
- Hirauchi, K. I., & Katayama, I. (2013). Rheological contrast between serpentine species and implications for slab-mantle wedge decoupling. *Tectonophysics*, 608, 545–551. <https://doi.org/10.1016/j.tecto.2013.08.027>
- Hilaret, N., Reynard, B., Wang, Y. B., Daniel, I., Merkel, S., Nishiyama, N., & Petitgirard, S. (2007). High-pressure creep of serpentinite, interseismic deformation, and initiation of subduction. *Science*, 318(5858), 1910–1913. <https://doi.org/10.1126/science.1148494>
- Hilaret, N., Wang, Y., Sanehira, T., Merkel, S., & Mei, S. (2011). Deformation of olivine under mantle conditions: An in-situ high-pressure, high-temperature study using monochromatic synchrotron radiation. *Journal of Geophysical Research*, 117(B1), B01203. <https://doi.org/10.1029/2011JB008498>
- Hirauchi, K. I., Katayama, I., & Kouketsu, Y. (2020). Semi-brittle deformation of antigorite serpentinite under forearc mantle wedge conditions. *Journal of Structural Geology*, 140, 104151. <https://doi.org/10.1016/j.jsg.2020.104151>
- Hirauchi, K.-I., Nagata, Y., Kataoka, K., Oyanagi, R., Okamoto, A., & Michibayashi, K. (2021). Cataclastic and crystal-plastic deformation in shallow mantle-wedge serpentinite controlled by cyclic changes in pore fluid pressures. *Earth and Planetary Science Letters*, 576, 117232. <https://doi.org/10.1016/j.epsl.2021.117232>
- Huet, B., Yamato, P., & Grasemann, B. (2014). The Minimized Power Geometric model: An analytical mixing model for calculating polyphase rock viscosities consistent with experimental data. *Journal of Geophysical Research: Solid Earth*, 119(4), 3897–3924. <https://doi.org/10.1002/2013jb010453>
- Idrissi, H., Bollinger, C., Boini, F., Schryvers, D., & Cordier, P. (2016). Low-temperature plasticity of olivine revisited with in situ TEM nanomechanical testing. *Science Advances*, 2(3), 6. <https://doi.org/10.1126/sciadv.1501671>
- Idrissi, H., Samaee, V., Lumbeck, G., van der Werf, T., Pardoën, T., Schryvers, D., & Cordier, P. (2020). In situ quantitative tensile testing of antigorite in a transmission electron microscope. *Journal of Geophysical Research: Solid Earth*, 125(3), e2019JB018383. <https://doi.org/10.1029/2019jb018383>
- Incel, S., Hilaret, N., Labrousse, L., John, T., Deldicque, D., Ferrand, T., et al. (2017). Laboratory earthquakes triggered during eclogitization of lawsonite-bearing blueschist. *Earth and Planetary Science Letters*, 459, 320–331. <https://doi.org/10.1016/j.epsl.2016.11.047>
- Isaak, D. G. (1992). High temperature elasticity of iron-bearing olivines. *Journal of Geophysical Research: Solid Earth*, 97(B2), 1871–1885. <https://doi.org/10.1029/91JB02675>
- Jessell, M. W., Bons, P. D., Griera, A., Evans, L. A., & Wilson, C. J. L. (2009). A tale of two viscosities. *Journal of Structural Geology*, 31(7), 719–736. <https://doi.org/10.1016/j.jsg.2009.04.010>
- Jung, H., & Green, H. W. (2004). Experimental faulting of serpentinite during dehydration: Implications for earthquakes, seismic low-velocity zones, and anomalous hypocenter distributions in subduction zones. *International Geology Review*, 46(12), 1089–1102. <https://doi.org/10.2747/0020-6814.46.12.1089>

- Kaercher, P., Miyagi, L., Kanitpanyacharoen, W., Zepeda-Alarcon, E., Wang, Y., Parkinson, D., et al. (2016). Two-phase deformation of lower mantle mineral analogs. *Earth and Planetary Science Letters*, *456*, 134–145. <https://doi.org/10.1016/j.epsl.2016.09.030>
- Karato, S.-i. (2008). *Deformation of Earth materials: An introduction to the rheology of solid Earth*. Cambridge University Press.
- Kranjc, K., Rouse, Z., Flores, K. M., & Skemer, P. (2016). Low-temperature plastic rheology of olivine determined by nanoindentation. *Geophysical Research Letters*, *43*(1), 176–184. <https://doi.org/10.1002/2015gl065837>
- Kumamoto, K. M., Thom, C. A., Wallis, D., Hansen, L. N., Armstrong, D. E. J., Warren, J. M., et al. (2017). Size effects resolve discrepancies in 40 years of work on low-temperature plasticity in olivine. *Science Advances*, *3*(9). <https://doi.org/10.1126/sciadv.1701338>
- Li, L., Addad, A., Weidner, D., Long, H. B., & Chen, J. H. (2007). High pressure deformation in two-phase aggregates. *Tectonophysics*, *439*(1–4), 107–117. <https://doi.org/10.1016/j.tecto.2007.04.004>
- Lin, F., Giannetta, M., Jugle, M., Couper, S., Dunleavy, B., & Miyagi, L. (2019). Texture development and stress-strain partitioning in periclase plus halite aggregates. *Minerals*, *9*(11), 679. <https://doi.org/10.3390/min9110679>
- Long, H., Weidner, D. J., Li, L., Chen, J., & Wang, L. (2011). Deformation of olivine at subduction zone conditions determined from in situ measurements with synchrotron radiation. *Physics of the Earth and Planetary Interiors*, *186*(1–2), 23–35. <https://doi.org/10.1016/j.pepi.2011.02.006>
- Madi, K., Forest, S., Cordier, P., & Boussuge, M. (2005). Numerical study of creep in two-phase aggregates with a large rheology contrast: Implications for the lower mantle. *Earth and Planetary Science Letters*, *237*(1–2), 223–238. <https://doi.org/10.1016/j.epsl.2005.06.027>
- Mei, S., Suzuki, A. M., Kohlstedt, D. L., Dixon, N. A., & Durham, W. B. (2010). Experimental constraints on the strength of the lithospheric mantle. *Journal of Geophysical Research*, *115*(B8), B08204. <https://doi.org/10.1029/2009jb006873>
- Merkel, S., & Hilairret, N. (2015). Multifit/polydefix: A framework for the analysis of polycrystal deformation using X-rays. *Journal of Applied Crystallography*, *48*(4), 1307–1313. <https://doi.org/10.1107/s1600576715010390>
- Merkel, S., Tome, C., & Wenk, H. R. (2009). Modeling analysis of the influence of plasticity on high pressure deformation of hcp-Co. *Physical Review B*, *79*(6), 064110. <https://doi.org/10.1103/PhysRevB.79.064110>
- Montési, L. G. J. (2013). Fabric development as the key for forming ductile shear zones and enabling plate tectonics. *Journal of Structural Geology*, *50*, 254–266. <https://doi.org/10.1016/j.jsg.2012.12.011>
- Montési, L. G. J., & Hirth, G. (2003). Grain size evolution and the rheology of ductile shear zones: From laboratory experiments to postseismic creep. *Earth and Planetary Science Letters*, *211*(1–2), 97–110. [https://doi.org/10.1016/S0012-821X\(03\)00196-1](https://doi.org/10.1016/S0012-821X(03)00196-1)
- Morales, L. F. G., Mainprice, D., & Kern, H. (2018). Olivine-antigorite orientation relationships: Microstructures, phase boundary misorientations and the effect of cracks in the seismic properties of serpentinites. *Tectonophysics*, *724*, 93–115. <https://doi.org/10.1016/j.tecto.2017.12.009>
- Nishii, A., Wallis, S. R., Mizukami, T., & Michibayashi, K. (2011). Subduction related antigorite CPO patterns from forearc mantle in the Sanbagawa belt, southwest Japan. *Journal of Structural Geology*, *33*(10), 1436–1445. <https://doi.org/10.1016/j.jsg.2011.08.006>
- Padron-Navarta, J. A., Tommasi, A., Garrido, C. J., & Sanchez-Vizcaino, V. L. (2012). Plastic deformation and development of antigorite crystal preferred orientation in high-pressure serpentinites. *Earth and Planetary Science Letters*, *349*, 75–86. <https://doi.org/10.1016/j.epsl.2012.06.049>
- Passchier, C. W., & Trouw, R. A. J. (2005). *Microtectonics, 2nd revised and enlarged edition, cop.* Springer.
- Peters, J. F., Muthuswamy, M., Wibowo, J., & Tordesillas, A. (2005). Characterization of force chains in granular material. *Physical Review*, *72*(4), 041307. <https://doi.org/10.1103/PhysRevE.72.041307>
- Proctor, B., & Hirth, G. (2016). "Ductile to brittle" transition in thermally stable antigorite gouge at mantle pressures. *Journal of Geophysical Research: Solid Earth*, *121*(3), 1652–1663. <https://doi.org/10.1002/2015jb012710>
- Proietti, A., Bystricky, M., Guignard, J., Béjina, F., & Crichton, W. (2016). Effect of pressure on the strength of olivine at room temperature. *Physics of the Earth and Planetary Interiors*, *259*, 34–44. <https://doi.org/10.1016/j.pepi.2016.08.004>
- Raterron, P., Merkel, S., & Holyoke, C. W., III. (2013). Axial temperature gradient and stress measurements in the deformation-DIA cell using alumina pistons. *Review of Scientific Instruments*, *84*(4), 43906. <https://doi.org/10.1063/1.4801956>
- Raterron, P., Wu, Y., Weidner, D. J., & Chen, J. (2004). Low-temperature olivine rheology at high pressure. *Physics of the Earth and Planetary Interiors*, *145*(1–4), 149–159. <https://doi.org/10.1016/j.pepi.2004.03.007>
- Regenauer-Lieb, K., & Yuen, D. A. (2008). Multiscale brittle-ductile coupling and genesis of slow earthquakes. *Pure and Applied Geophysics*, *165*(3–4), 523–543. <https://doi.org/10.1007/s00024-008-0326-8>
- Schmidt, M. W., & Poli, S. (1998). Experimentally based water budgets for dehydrating slabs and consequences for arc magma generation. *Earth and Planetary Science Letters*, *163*(1–4), 361–379. [https://doi.org/10.1016/S0012-821X\(98\)00142-3](https://doi.org/10.1016/S0012-821X(98)00142-3)
- Schwartz, S., Allemand, P., & Guillot, S. (2001). Numerical model of the effect of serpentinites on the exhumation of eclogitic rocks: Insights from the Monviso ophiolitic massif (Western Alps). *Tectonophysics*, *342*(1–2), 193–206. [https://doi.org/10.1016/S0040-1951\(01\)00162-7](https://doi.org/10.1016/S0040-1951(01)00162-7)
- Schwartz, S., Guillot, S., Reynard, B., Lafay, R., Debret, B., Nicollet, C., et al. (2013). Pressure-temperature estimates of the lizardite/antigorite transition in high pressure serpentinites. *Lithos*, *178*, 197–210. <https://doi.org/10.1016/j.lithos.2012.11.023>
- Shao, T. B., Zhou, Y. S., Song, M. S., Ma, X., Zhang, L., Yao, W. M., et al. (2021). Deformation of antigorite and its geological implications. *Journal of Geophysical Research: Solid Earth*, *126*(6), e2021JB021650. <https://doi.org/10.1029/2021JB021650>
- Shimada, M., Cho, A., & Yukutake, H. (1983). Fracture strength of dry silicate rocks at high confining pressures and activity of acoustic emission. *Tectonophysics*, *96*(1–2), 159–172. [https://doi.org/10.1016/0040-1951\(83\)90248-2](https://doi.org/10.1016/0040-1951(83)90248-2)
- Singh, A. K., Balasingh, C., Mao, H. K., Hemley, R. J., & Shu, J. F. (1998). Analysis of lattice strains measured under nonhydrostatic pressure. *Journal of Applied Physics*, *83*(12), 7567–7575. <https://doi.org/10.1063/1.367872>
- Takeda, Y. T. (1998). Flow in rocks modelled as multiphase continua: Application to polymineralic rocks. *Journal of Structural Geology*, *20*(11), 1569–1578. [https://doi.org/10.1016/S0191-8141\(98\)00043-1](https://doi.org/10.1016/S0191-8141(98)00043-1)
- Thielmann, M., Golabek, G. J., & Marquardt, H. (2020). Ferropericlase control of lower mantle rheology: Impact of phase morphology. *Geochemistry, Geophysics, Geosystems*, *21*(2), e2019GC008688. <https://doi.org/10.1029/2019GC008688>
- Tokle, L., Hirth, G., Liang, Y., Raterron, P., & Dygert, N. (2021). The effect of pressure and Mg-content on ilmenite rheology: Implications for lunar cumulate mantle overturn. *Journal of Geophysical Research: Planets*, *126*(1), e2020JE006494. <https://doi.org/10.1029/2020JE006494>
- Tullis, T. E., Horowitz, F. G., & Tullis, J. (1991). Flow laws of polyphase aggregates from end-member flow laws. *Journal of Geophysical Research: Solid Earth*, *96*(B5), 8081–8096. <https://doi.org/10.1029/90jb02491>
- Uchida, T., Funamori, N., & Yagi, T. (1996). Lattice strains in crystals under uniaxial stress field. *Journal of Applied Physics*, *80*(2), 739–746. <https://doi.org/10.1063/1.362920>
- Wada, I., Wang, K., He, J., & Hyndman, R. D. (2008). Weakening of the subduction interface and its effects on surface heat flow, slab dehydration, and mantle wedge serpentinization. *Journal of Geophysical Research: Solid Earth*, *113*(B4), B04402. <https://doi.org/10.1029/2007JB005190>

- Wallis, S. R., Kobayashi, H., Nishii, A., Mizukami, T., & Seto, Y. (2011). Obliteration of olivine crystallographic preferred orientation patterns in subduction-related antigorite-bearing mantle peridotite: An example from the Higashi–Akaishi body, SW Japan. In D. J. Prior, E. H. Rutter, & D. J. Tatham (Eds.), *Deformation mechanisms, rheology and tectonics: Microstructures, mechanics and anisotropy* (Vol. 360, pp. 113–127). Geological Society, London, Special Publications. <https://doi.org/10.1144/SP360.7>
- Wang, Y., Hilairet, N., Nishiyama, N., Yahata, N., Tsuchiya, T., Morard, G., & Fiquet, G. (2013). High-pressure, high-temperature deformation of CaGeO<sub>3</sub> (perovskite)±MgO aggregates: Implications for multiphase rheology of the lower mantle. *Geochemistry, Geophysics, Geosystems*, 14(9), 3389–3408. <https://doi.org/10.1002/ggge.20200>
- Xia, G. (2013). Experimental studies on dehydration embrittlement of serpentinized peridotite and effect of pressure on creep of olivine (Doctoral dissertation). University of California.
- Zha, C. S., Duffy, T. S., Downs, R. T., Mao, H. K., & Hemley, R. J. (1996). Sound velocity and elasticity of single-crystal forsterite to 16 GPa. *Journal of Geophysical Research: Solid Earth*, 101(B8), 17535–17545. <https://doi.org/10.1029/96JB01266>

### References From the Supporting Information

- Lloyd, G. E., Farmer, A. B., & Mainprice, D. (1997). Misorientation analysis and the formation and orientation of subgrain and grain boundaries. *Tectonophysics*, 279(1–4), 55–78. [https://doi.org/10.1016/S0040-1951\(97\)00115-7](https://doi.org/10.1016/S0040-1951(97)00115-7)
- Lutterotti, L., Bortolotti, M., Ischia, G., Lonardelli, I., & Wenk, H.-R. (2007). Rietveld texture analysis from diffraction images. *Zeitschrift für Kristallographie Supplements*, 2007(Suppl 26), 125–130. [https://doi.org/10.1524/zksu.2007.2007.suppl\\_26.125](https://doi.org/10.1524/zksu.2007.2007.suppl_26.125)